

1 **The Education and Research 3D Radiative Transfer Toolbox (EaR³T) – Towards the**
2 **Mitigation of 3D Bias in Airborne and Spaceborne Passive Imagery Cloud Retrievals**

3

4 Hong Chen^{1,2}, K. Sebastian Schmidt^{1,2}, Steven T. Massie², Vikas Nataraja², Matthew S. Norgren²,
5 Jake J. Gristey^{3,4}, Graham Feingold⁴, Robert E. Holz⁵, Hironobu Iwabuchi⁶

6

7

8 ¹Department of Atmospheric and Oceanic Sciences, University of Colorado, Boulder, CO, USA

9 ²Laboratory for Atmospheric and Space Physics, University of Colorado, Boulder, CO, USA

10 ³Cooperative Institute for Research in Environmental Sciences, University of Colorado,
11 Boulder, CO, USA

12 ⁴NOAA Chemical Sciences Laboratory, Boulder, CO, USA

13 ⁵Space Science and Engineering Center, University of Wisconsin–Madison, Madison, WI, USA

14 ⁶Center for Atmospheric and Oceanic Studies, Tohoku University, Sendai, Miyagi, Japan

15

16

17

18

19 *Correspondence to:* Hong Chen (hong.chen-1@colorado.edu)

20 **Abstract**

21 We introduce the Education and Research 3D Radiative Transfer Toolbox (EaR³T) for quantifying
22 and mitigating artifacts in atmospheric radiation science algorithms due to spatially inhomogeneous clouds
23 and surfaces, and show the benefits of automated, realistic radiance and irradiance generation along
24 extended satellite orbits, flight tracks from entire aircraft field missions, and synthetic data generation from
25 model data. EaR³T is a modularized Python package that provides high-level interfaces to automate the
26 process of 3D radiative transfer (RT) calculations. After introducing the package, we present initial findings
27 from four applications, which are intended as blueprints to future in-depth scientific studies. The first two
28 applications use EaR³T as a satellite radiance simulator for the NASA Orbiting Carbon Observatory 2
29 (OCO-2) and Moderate Resolution Imaging Spectroradiometer (MODIS) missions, which generate
30 synthetic satellite observations with 3D-RT on the basis of cloud field properties from imagery-based
31 retrievals and other input data. In the case of inhomogeneous cloud fields, we show that the synthetic
32 radiances are often inconsistent with the original radiance measurements. This lack of radiance consistency
33 points to biases in heritage imagery cloud retrievals due to sub-pixel resolution clouds and 3D-RT effects.
34 They come to light because the simulator’s 3D-RT engine replicates processes in nature that conventional
35 1D-RT retrievals do not capture. We argue that 3D radiance consistency (closure) can serve as a metric for
36 assessing the performance of a cloud retrieval in presence of spatial cloud inhomogeneity even with limited
37 independent validation data. The other two applications show how airborne measured irradiance data can
38 be used to independently validate imagery-derived cloud products via radiative closure in irradiance. This
39 is accomplished by simulating downwelling irradiance from geostationary cloud retrievals of Advanced
40 Himawari Imager (AHI) along all the below-cloud aircraft flight tracks of the Cloud, Aerosol and Monsoon
41 Processes Philippines Experiment (CAMP²Ex, NASA 2019), and comparing the irradiances with the
42 collocated airborne measurements. In contrast to isolated case studies in the past, EaR³T facilitates the use
43 of observations from entire field campaigns for the statistical validation of satellite-derived irradiance. From
44 the CAMP²Ex mission, we find a low bias of 10% in the satellite-derived cloud transmittance, which we
45 are able to attribute to a combination of the coarse resolution of the geostationary imager and 3D-RT biases.
46 Finally, we apply a recently developed context-aware Convolutional Neural Network (CNN) cloud retrieval
47 framework to high-resolution airborne imagery from CAMP²Ex and show that the retrieved cloud optical
48 thickness fields lead to better 3D radiance consistency than the heritage independent pixel algorithm,
49 opening the door to future mitigation of 3D-RT cloud retrieval biases.

50 **1. Introduction**

51 Three-dimensional cloud effects in imagery-derived cloud properties have long been
52 considered an unavoidable error source when estimating the radiative effect of clouds and aerosols.
53 Consequently, research efforts involving satellite, aircraft, and surface observations in conjunction
54 with modeled clouds and radiative transfer calculations have focused on systematic bias
55 quantification under different atmospheric conditions. Barker and Liu (1995) studied the so-called
56 independent pixel approximation (IPA) bias in cloud optical thickness (COT) retrievals from
57 shortwave cloud reflectance. The bias arises when approximating the radiative transfer relating to
58 COT and measured reflectance at the pixel or cloud column level through one-dimensional (1D)
59 radiative transfer (RT) calculations, while ignoring its radiative context. However, net horizontal
60 photon transport and other effects such as shading engender column-to-column radiative
61 interactions that can only be captured in a three-dimensional (3D) framework, and can be regarded
62 as a 3D perturbation or bias relative to the 1D-RT (IPA) baseline. 3D biases affect not only cloud
63 remote sensing but they also propagate into the derived irradiance fields and cloud radiative effects
64 (CRE). Since the derivation of regional and global CRE relies heavily on satellite imagery, any
65 systematic 3D bias impacts the accuracy of the Earth's radiative budget. Likewise, imagery-based
66 aerosol remote sensing in the vicinity of clouds can be biased by net horizontal photon transport
67 (Marshak et al., 2008). Additionally, satellite shortwave spectroscopy retrievals of CO₂ mixing
68 ratio are affected by nearby clouds (Massie et al., 2017), albeit through a different physical
69 mechanism than in aerosol and cloud remote sensing (Schmidt et al., 2022).

70 Given the importance of 3D perturbations for atmospheric remote sensing, ongoing
71 research seeks to mitigate the 3D effects. Cloud tomography, for example, inverts multi-angle
72 radiances to infer the 3D cloud extinction distribution (Levis et al., 2020). This is achieved through
73 iterative adjustments to the cloud field until the calculated radiances match the observations.
74 Convolutional neural networks (CNNs, Masuda et al., 2019; Nataraja et al., 2022) account for
75 3D-RT perturbations in COT retrievals through pattern-based machine learning that operates on
76 collections of imagery pixels, rather than treating them in isolation like IPA. Unlike tomography,
77 CNNs require training based on extensive cloud-type specific synthetic data with the ground truth
78 of cloud optical properties and their associated radiances from 3D-RT calculations. Once the
79 CNNs are trained, they do not require real-time 3D-RT calculations and can therefore be useful in
80 an operational setting. Whatever the future may hold for context-aware multi-pixel or multi-sensor

81 cloud retrievals, there is a paradigm shift on the horizon that started when the radiation concept
82 for the Earth Clouds, Aerosol and Radiation Explorer (EarthCARE, Illingworth et al., 2015) was
83 first proposed (Barker et al., 2012). It foresees a closure loop where broadband radiances, along
84 with irradiance, are calculated in a 3D-RT framework from multi-sensor input fields (Barker et al.,
85 2011), and subsequently compared to independent observations by radiometers pointing in three
86 directions (nadir, forward-, and backward-viewing along the orbit). This built-in radiance closure
87 can serve as an accuracy metric for any downstream radiation products such as heating rates and
88 CRE. Any inconsistencies can be used to nudge the input fields towards the truth in subsequent
89 loop iterations akin to optimal estimation, or propagated into uncertainties of the cloud and
90 radiation products.

91 This general approach to radiative closure is also being considered for the National
92 Aeronautics and Space Administration (NASA) Atmospheric Observation System (AOS,
93 developed under the A-CCP, Aerosol and Cloud, Convection and Precipitation study), a mission
94 that is currently in its early implementation stages. Owing to its focus on studying
95 aerosol-cloud-precipitation-radiation interactions at the process level, it requires radiation
96 observables at a finer spatial resolution than achieved with missions to date. At target scales close
97 to 1 km, 3D-RT effects are much more pronounced than at the traditional 20 km scale of NASA
98 radiation products (O’Hirok and Gautier, 2005; Ham et al., 2014; Song et al., 2016; Gristey et al.,
99 2020a). Since this leads to biases beyond the desired accuracy of the radiation products, mitigation
100 of 3D-RT cloud remote sensing biases needs to be actively pursued over the next few years.

101 Transitioning to an explicit treatment of 3D-RT in operational approaches entails a new
102 generation of code architectures that can be easily configured for various instrument constellations,
103 interlink remote sensing parameters with irradiances, heating rates, and other radiative effects, and
104 can be used for automated processing of large data quantities. A number of 3D solvers are available
105 for different purposes, for example, the I3RC (International Intercomparison of 3D Radiation
106 Codes: Cahalan et al., 2005) community Monte Carlo code¹, which now also includes an online
107 simulator² (Gatebe et al., 2021); MCarATS (Monte Carlo Atmospheric Radiative Transfer
108 Simulator³: Iwabuchi, 2006); MYSTIC (Monte Carlo code for the physically correct tracing of

¹ <https://earth.gsfc.nasa.gov/climate/model/i3rc>, last accessed on 26 November, 2022.

² <http://i3rcsimulator.umbc.edu>, last accessed on 26 November, 2022.

³ <https://sites.google.com/site/mcarats/monte-carlo-atmospheric-radiative-transfer-simulator-mcarats>, last accessed on 26 November, 2022.

109 photons in cloudy atmospheres: Mayer, 2009), which is embedded in libRadtran (library for
110 radiative transfer, Mayer and Kylling, 2005); McSCIA (Monte Carlo [RT] for SCIAMachy: Spada
111 et al., 2006), which is optimized for satellite radiance simulations (including limb-viewing) in a
112 spherical atmosphere; McARTIM (Deutschmann et al., 2011), with several hyperspectral
113 polarimetric applications such as differential optical absorption spectroscopy; and SHDOM
114 (Spherical Harmonic Discrete Ordinate Method⁴: Evans, 1998), which, unlike the other methods,
115 is a deterministic solver with polarimetric capabilities (Doicu et al., 2013; Emde et al., 2015) that
116 is differentiable and can therefore be used for tomography (Loveridge et al., 2022).

117 For the future operational application of 3D-RT, it is, however, desirable to run various
118 different solvers in one common architecture that automates the processing of various formats of
119 3D atmospheric input fields (including satellite data), allows the user to choose from various
120 options for atmospheric absorption and scattering, and simulates radiance and irradiance data for
121 real-world scenes. Here, we introduce one such tool that could serve as the seed for this architecture:
122 the Education and Research 3D Radiative Transfer Toolbox (EaR³T). It has been developed over
123 the past few years at the University of Colorado to automate 3D-RT calculations based on imagery
124 or model cloud fields with minimal user input. EaR³T is maintained and extended by graduate
125 students as part of their education, and applied to various different research projects including
126 machine learning for atmospheric radiation and remote sensing (Gristey et al., 2020b; 2022;
127 Nataraja et al., 2022), as well as radiative closure and satellite simulators (this paper and Schmidt
128 et al., 2022). It is implemented as a modularized Python package with various application codes
129 that combine the functionality in different ways, which, once set up, autonomously process large
130 amounts of data required by airborne and satellite remote sensing and for machine learning
131 applications.

132 The goal of the paper is to introduce EaR³T as a versatile tool for systematically quantifying
133 and mitigating 3D cloud effects in radiation science as foreseen in future missions. To do so, we
134 will first showcase EaR³T as an automated radiance simulator for two satellite instruments, the
135 Orbiting Carbon Observatory-2 (OCO-2, this application is referred to as App. 1 in this manuscript)
136 and the Moderate Resolution Imaging Spectroradiometer (MODIS, application code 2, App. 2)
137 from publicly available satellite retrieval products. In the spirit of radiance closure, the intended
138 use is the comparison of modeled radiances with the original measurements to assess the accuracy

⁴ <https://coloradolinux.com/shdom>, last accessed on 26 November, 2022.

139 of the input data, as follows: operational IPA COT products are made using 1D-RT, and thus the
140 accompanying radiances are consistent with the original measurements under that 1D-RT
141 assumption only. That is, self-consistency is assured if 1D-RT is used in both the inversion and
142 radiance simulation. However, since nature creates 3D-RT radiation fields, we break this
143 traditional symmetry in this manuscript and introduce the concept of 3D radiance consistency
144 where closure is only achieved if the original measurements are consistent with the 3D-RT (rather
145 than the 1D-RT) simulations. The level of inconsistency is then used as a metric for the magnitude
146 of 3D-RT retrieval artifacts as envisioned by the architects of the EarthCARE radiation concept
147 (Barker et al., 2012).

148 Subsequently, we discuss applications where EaR³T performs radiative closure in the
149 traditional sense, i.e., between irradiances derived from satellite products and collocated airborne
150 or ground-based observations. The aircraft Cloud, Aerosol and Monsoon Processes Philippines
151 Experiment (CAMP²Ex, Reid et al., 2022), conducted by NASA in the Philippines in 2019, serves
152 as a testbed of this approach. Here, we use EaR³T's automated processing capabilities to derive
153 irradiance from geostationary imagery cloud products and then compare these to cumulative
154 measurements made along all flight legs of the campaign (application code 3, App. 3). In contrast
155 to previous studies that often rely on a number of cases (e.g., Schmidt et al., 2010; Kindel et al.,
156 2010), we perform closure systematically for the entire data set, enabling us to identify 3D-RT
157 biases in a statistically significant manner. Finally, we apply a regionally and cloud type specific
158 CNN, introduced by Nataraja et al. (2022) that is included with the EaR³T distribution, to high-
159 resolution camera imagery from CAMP²Ex. This last example demonstrates mitigation of 3D-RT
160 biases in cloud retrievals using the concept of radiance closure to quantify its performance against
161 the baseline IPA (application code 4).

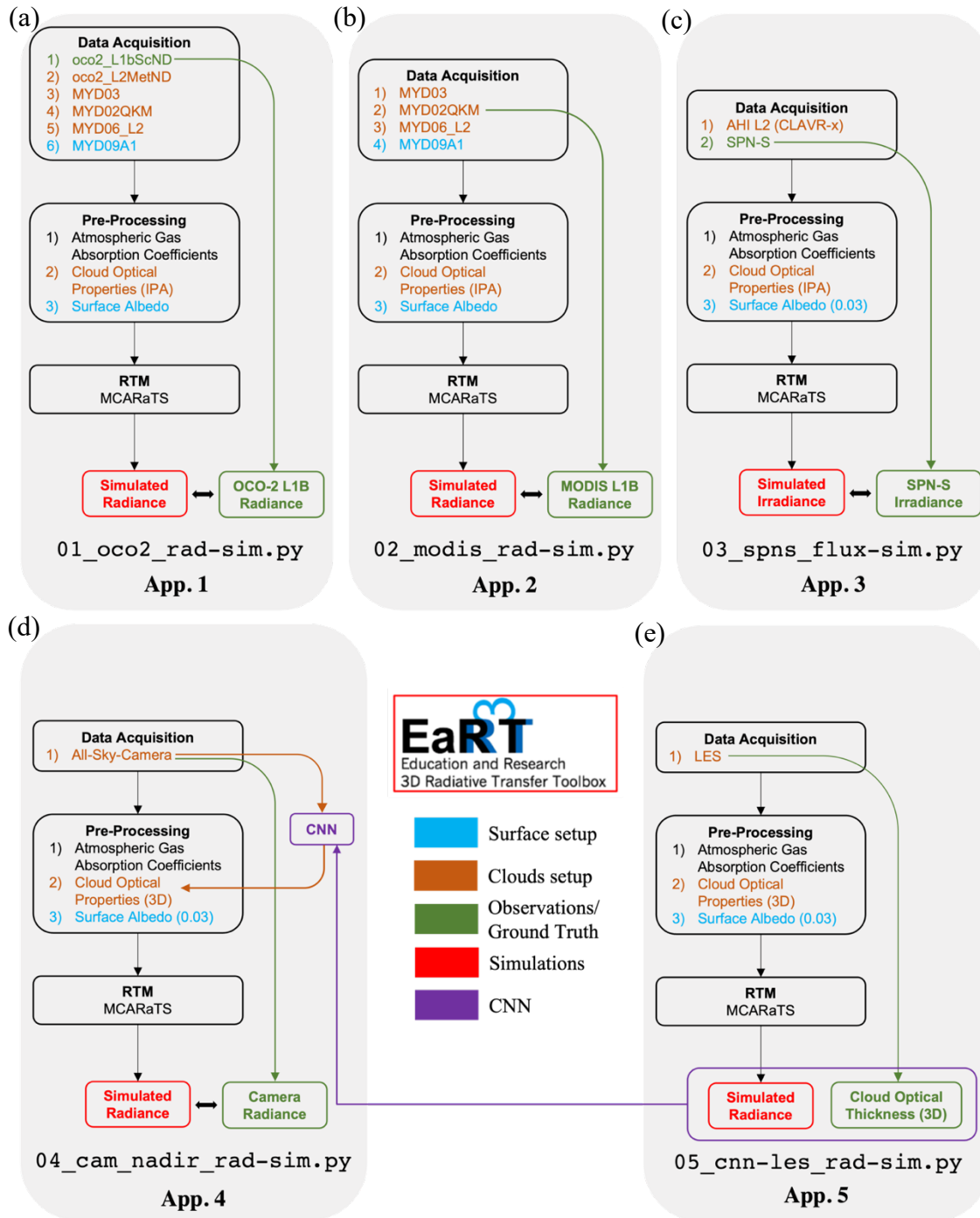
162 The general concept of EaR³T with an overview of the applications, along with the data
163 used for both parts of the paper is presented in section 2, followed by a description of the
164 procedures of EaR³T in section 3. Results for the OCO-2 and MODIS satellite simulators (part 1)
165 are shown in section 4, followed by the quantification and mitigation of 3D-RT biases with
166 CAMP²Ex data in section 5 and section 6 (part 2). A summary and conclusion are provided in
167 section 7. The code, along with the applications presented in this paper, can be downloaded from
168 the GitHub repository: <https://github.com/hong-chen/er3t>.

169

170 **2. Functionality and Data Flow within EaR³T**

171 **2.1 Overview**

172 To introduce EaR³T as a satellite radiance simulator tool and to demonstrate its use for the
 173 quantification and mitigation of 3D cloud remote sensing biases, five applications (Figure 1) are
 174 included in the GitHub software release, four of which are discussed in this paper:
 175



176

177 **Figure 1.** Flow charts of EaR³T applications for (a) OCO-2 radiance simulation at 768.52 nm (data described in section
178 2.2.1 and 2.2.2, results discussed in section 4), (b) MODIS radiance simulation at 650 nm (data described
179 in section 2.2.1, results discussed in section 4), (c) SPN-S irradiance simulation at 745 nm (data described
180 in section 2.2.3 and 2.2.4, results discussed in section 5), (d) all-sky camera radiance simulation at 600 nm
181 (data described in section 2.2.5, results discussed in section 6), and (e) radiance simulation at 600 nm based
182 on LES data for CNN training (Appendix B). The data products and their abbreviations are described in
183 section 2.2.

- 184
- 185 1. App. 1, section 4.1 (`examples/01_oco2_rad-sim.py`): Radiance simulations along
186 the track of OCO-2, based on data products from MODIS and others – to assess consistency
187 (closure) between simulated and measured radiance;
- 188 2. App. 2, section 4.2 (`examples/02_modis_rad-sim.py`): MODIS radiance
189 simulations – to assess self-consistency of MODIS level-2 (L2) products with the
190 associated radiance fields (LIB product) under spatially inhomogeneous conditions;
- 191 3. App. 3, section 5 (`examples/03_spns_flux-sim.py`): Irradiance simulations along
192 aircraft flight tracks, utilizing the L2 cloud products of the AHI, and comparison with
193 aircraft measurements – to quantify retrieval biases due to 3D cloud structure based with
194 data from an entire aircraft field campaign;
- 195 4. App. 4, section 6 (`examples/04_cam_nadir_rad-sim.py`): Mitigation of 3D
196 cloud biases in passive imagery COT retrievals from an airborne camera, application of a
197 convolutional neural network (CNN) and subsequent comparison of CNN-derived
198 radiances with the original measurements – to illustrate how the radiance self-consistency
199 concept assesses the fidelity of cloud retrievals.
- 200 5. App. 5, Appendix B (`examples/05_cnn-les_rad-sim.py`): Generation of training
201 data for the CNN (App. 4) based on LES inputs. The training datasets contains 1) the
202 ground truth of COT from the LES data; 2) realistic radiance simulated by EaR³T based on
203 the LES cloud fields.

204 Figure 1 shows the high-level workflow of the applications. The first four share the general
205 concept of evaluating simulations (the output from the EaR³T, indicated in red at the bottom of
206 each column) with observations (indicated in green at the bottom) from various satellite and
207 aircraft instruments. The results for the first four applications are interpreted in section 4.1, section
208 4.2, section 5, and section 6. The results for App. 5 are discussed in detail in a separate paper by

209 Nataraja et al. (2022). In this paper, we will only provide a brief description for App. 5 in Appendix
210 B. The workflow of each application consists of three parts – 1) data acquisition, 2) pre-processing,
211 and 3) RTM setup and execution. EaR³T includes functions to ingest data from various different
212 sources, e.g., satellite data from publicly available data archives, which can be combined in
213 different ways to accommodate input data depending on the application specifics. For example, in
214 App. 1, EaR³T is used to automatically download and process MODIS and OCO-2 data files based
215 on the user-specified region, date and time. Building on the templates provided in the current code
216 distribution, the functionality can be extended to new spaceborne or airborne instruments. The fifth
217 column of Figure 1 shows an application that differs from the first four, and was developed for
218 earlier papers (Gristey et al., 2020a and 2020b; Nataraja et al., 2022; Gristey et al., 2022). In
219 contrast to the first four, which use imagery products as input, the fifth application ingests model
220 output from a Large Eddy Simulation (LES) and produces irradiance data for surface energy
221 budget applications, or synthetic radiance fields for training a CNN. Details and results are
222 described in the respective papers. Furthermore, Schmidt et al. (2022) builds upon App. 1 to study
223 the mechanism of 3D cloud biases in OCO-2 passive spectroscopy retrievals.

224 After the required data files have been downloaded in the data acquisition step, EaR³T
225 pre-processes them and generates the optical properties of atmospheric gases, clouds, aerosols, and
226 the surface. In Figure 1, the mapping from input data to these properties is color-coded
227 component-wise (brown for associated cloud property processing if available, blue for associated
228 surface property processing if available, green for associated ground truth property). The version
229 used in this paper (v0.1.0; Chen and Schmidt, 2022) only includes MCARaTS as the 3D RT solver,
230 but others are planned for the future. MCARaTS is a radiative transfer solver uses Monte Carlo
231 photon-tracing method (Iwabuchi, 2006). It outputs radiation (radiance or irradiance) based on the
232 inputs of radiative properties of surface and atmospheric constituents (e.g., gases, aerosols, clouds)
233 such as single scattering albedo, scattering phase function, or asymmetry parameters, along with
234 solar and sensor viewing geometries. The setup of these input properties is implemented in
235 EaR³T's pre-processing steps, which translates atmospheric properties into solver-specific input
236 with minimum user intervention. To achieve this, EaR³T is modular so that it can be extended as
237 new solvers are added. Although the five specific applications in this paper do not include aerosol
238 layers, the setup of aerosol fields is fully supported and has been used in other applications (e.g.,
239 Gristey et al., 2022). After pre-processing, the optical properties are fed into the RT solver. Finally,

240 the user obtains radiation output from EaR³T, either radiance or irradiance. The output is saved in
 241 HDF5 format and can be easily distributed and accessed by various programming languages. The
 242 data variables contained in the HDF5 output are provided in Table 1.
 243

Metadata			
Variable Name	Description	Data Type	Dimension
mean/N_photon	Number of photons per run	Array	N_g
mean/N_run	Number of runs	Integer value	N/A
mean/toa	TOA downwelling flux	Float value	N/A
Radiance			
Variable Name	Description	Data Type	Dimension
mean/rad	Radiance field at user specified altitude averaged over different runs	Array	(N_x, N_y)
mean/rad_std	Standard deviation of the radiance fields from different runs	Array	(N_x, N_y)
Irradiance			
Variable Name	Description	Data Type	Dimension
mean/f_down	Downwelling irradiance averaged over different runs	Array	(N_x, N_y, N_z)
mean/f_down_std	Standard deviation of the downwelling irradiance from different runs	Array	(N_x, N_y, N_z)
mean/f_down_diffuse	Diffuse downwelling irradiance averaged over different runs	Array	(N_x, N_y, N_z)
mean/f_down_diffuse_std	Standard deviation of the diffuse downwelling irradiance from different runs	Array	(N_x, N_y, N_z)

mean/f_down_direct	Direct downwelling irradiance averaged over different runs	Array	(N_x, N_y, N_z)
mean/f_down_direct_std	Standard deviation of the direct downwelling irradiance from different runs	Array	(N_x, N_y, N_z)
mean/f_up	Upwelling irradiance averaged over different runs	Array	(N_x, N_y, N_z)
mean/f_up_std	Standard deviation of the upwelling irradiance from different runs	Array	(N_x, N_y, N_z)

244

245 **Table 1:** Data variables contained in the output HDF5 file from EaR³T for radiance and irradiance calculations. The
 246 radiance is simulated with a user-specified sensor geometry at a given altitude using forward photon tracing.
 247 The data variables listed under Metadata are included for both radiance and irradiance calculations. N_x,
 248 N_y, and N_z are the number of pixels along x, y, and z direction, respectively. N_g is the number of g,
 249 explained in section 3 – Correlated-k.

250

251 The aforementioned three steps – data acquisition, pre-processing, and RTM setup and
 252 execution are automated such that the 3D/1D-RT calculations can be performed for any region at
 253 any date and time using satellite or aircraft data or other data resources such as LES. EaR³T is
 254 hosted on GitHub at <https://www.github.com/hong-chen/er3t>. Since it is developed as an
 255 educational and research 3D-RT tool collection by students, it is a living code base, intended to be
 256 updated over time. The master code modules for the five applications as listed in Figure 1 are
 257 included in the EaR³T package under the `examples` directory. In the current release (v0.1.0),
 258 only a limited documentation for the installation and usage, including example codes for EaR³T,
 259 are provided. More effort will be dedicated for documentation in the near-future.

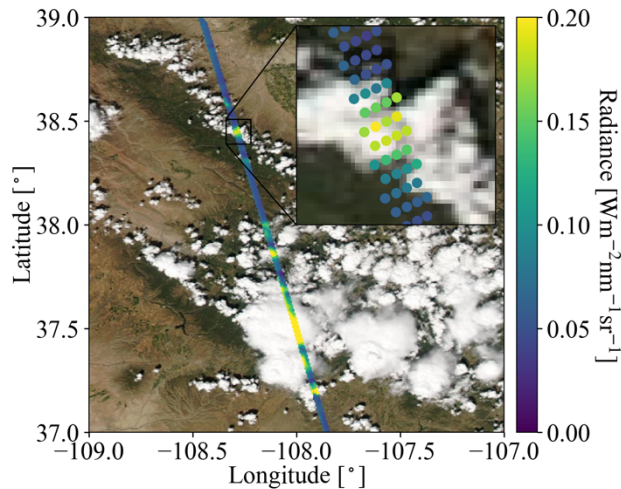
260

261 2.2 Data

262 The radiance simulations in App. 1 and App. 2 use data from the OCO-2 and MODIS-Aqua
 263 instruments, both of which are in a sun-synchronous polar orbit with an early-afternoon equator
 264 crossing time within NASA’s A-Train satellite constellation. Figure 2 visualizes radiance
 265 measurements by OCO-2 in the context of MODIS Aqua imagery over a partially vegetated and

266 partially cloud-covered land, illustrating that MODIS provides imagery and scene context for
 267 OCO-2, which in turn observes radiances from a narrow swath. The region is located in southwest
 268 Colorado in the United States of America. We selected this case because both the surface and
 269 clouds are varied along with diverse surface types. The surface features green forest and brown
 270 soil, whereas clouds include small cumulus and large cumulonimbus. In addition, this scene
 271 contains relatively homogeneous cloud fields in the north and inhomogeneous cloud fields in the
 272 south, which allows us to evaluate the simulations from various aspects of cloud morphology. To
 273 simulate the radiances of both instruments we use data products from OCO-2 and MODIS, as well
 274 as reanalysis products from NASA’s Global Modeling and Assimilation Office (GMAO) sampled
 275 at OCO-2 footprints and distributed along with OCO-2 data (section 2.2.2).

276



277
 278 **Figure 2.** OCO-2 measured radiance (units: $\text{Wm}^{-2}\text{nm}^{-1}\text{sr}^{-1}$) at 768.52 nm, overlaid on MODIS Aqua RGB imagery
 279 over southwestern Colorado (USA) on 2 September, 2019. The inset shows an enlarged portion along the
 280 track, illustrating that OCO-2 radiances co-vary with MODIS-Aqua radiance observations.

281

282 For App. 3 (irradiance simulations and 3D cloud bias quantification), we use geostationary
 283 imagery from the Japanese Space Agency’s Advanced Himawari Imager to provide cloud
 284 information in the area of the flight path of the NASA CAMP²Ex aircraft (Reid et al., 2022). The
 285 AHI data are used in conjunction with aircraft measurements of shortwave spectral radiation
 286 (section 2.2.4). Subsequently (App. 4: 3D cloud bias mitigation), we demonstrate the concept of
 287 radiance closure under partially cloudy conditions with airborne camera imagery (section 2.2.5).
 288 The underlying cloud retrieval is based on a convolutional neural network (CNN), which is

289 described in a related paper (Nataraja et al., 2022) in this special issue and relies on EaR³T-
290 generated synthetic radiance data based on Large Eddy Simulations (LES).

291

292 **2.2.1 Moderate Resolution Imaging Spectroradiometer (MODIS)**

293 The MODIS instruments are multi-use multispectral radiometers onboard NASA's Terra
294 and Aqua satellites, which were launched in 1999 and 2002 respectively. MODIS was conceived
295 as a central element of the Earth Observing System (EOS, King and Platnick, 2018). For App. 1
296 and App. 2, EaR³T ingests MODIS level 1B radiance products at the quarter kilometer scale
297 (channels 1 and 2, bands centered at 650 and 860 nm), MxD02QKM, where 'x' stands for 'O' in
298 the case of MODIS on Terra, and 'Y' in the case of Aqua data), the geolocation product (MxD03),
299 the level 2 cloud product (MxD06), and the surface reflectance product (MxD09A1). For this paper,
300 we use only Aqua data (MYD), from data collection 6.1. All the data are publicly available, and
301 are distributed at the LAADS (Level-1 and Atmosphere Archive & Distribution System)
302 Distributed Active Archive Center (DAAC) by NASA's Goddard Space Flight Center.

303 For cloud properties in App. 2, we use the MODIS cloud product (MxD06L2, collection
304 6.1). It provides cloud properties such as cloud optical thickness (COT), cloud effective radius
305 (CER), cloud thermodynamic phase, cloud top height (CTH), etc. (Nakajima and King, 1990;
306 Platnick et al., 2003). Since 3D cloud effects such as horizontal photon transport are most
307 significant at small spatial scales (e.g., Song et al., 2016), we use the high-resolution red (650 nm)
308 channel 1 (250 m), and derive COT directly from the reflectance in the Level-1B data
309 (MYD02QKM) instead of using the coarser-scale operational product from MYD06. CER and
310 CTH are sourced from MYD06 and re-gridded to 250 m. The EaR³T strategy for MODIS data is
311 similar, in principle, to the more advanced method by Deneke et al. (2021), which uses a
312 high-resolution wide-band visible channel from geostationary imagery to up-sample narrow-band
313 coarse-resolution channels. However, we simplified cloud detection and derivation of COT from
314 reflectance data for the purpose of our paper by using a threshold method (Appendix C1) and the
315 two-stream approximation (Appendix C2). In future versions of EaR³T this will be upgraded to
316 more sophisticated algorithms. A simple algorithm (Appendix D1) is used to correct for the
317 parallax shift based on the sensor geometries and cloud heights. The cloud top height data is
318 provided by the MODIS L2 cloud product and assuming cloud base is the same.

319 For the surface albedo required by the RTM, we used MYD09A1, which provides
320 cloud-cleared surface reflectance observations aggregated over an 8-day period (Vermote et al.,
321 2015). This product is available on a sinusoidal grid with a spatial resolution of 500 m for MODIS
322 band 2, and includes atmospheric correction for gas and aerosol scattering and absorption.
323 Assuming a Lambertian surface in this first release of EaR³T, we used surface reflectance as
324 surface albedo input to the RTM.

325

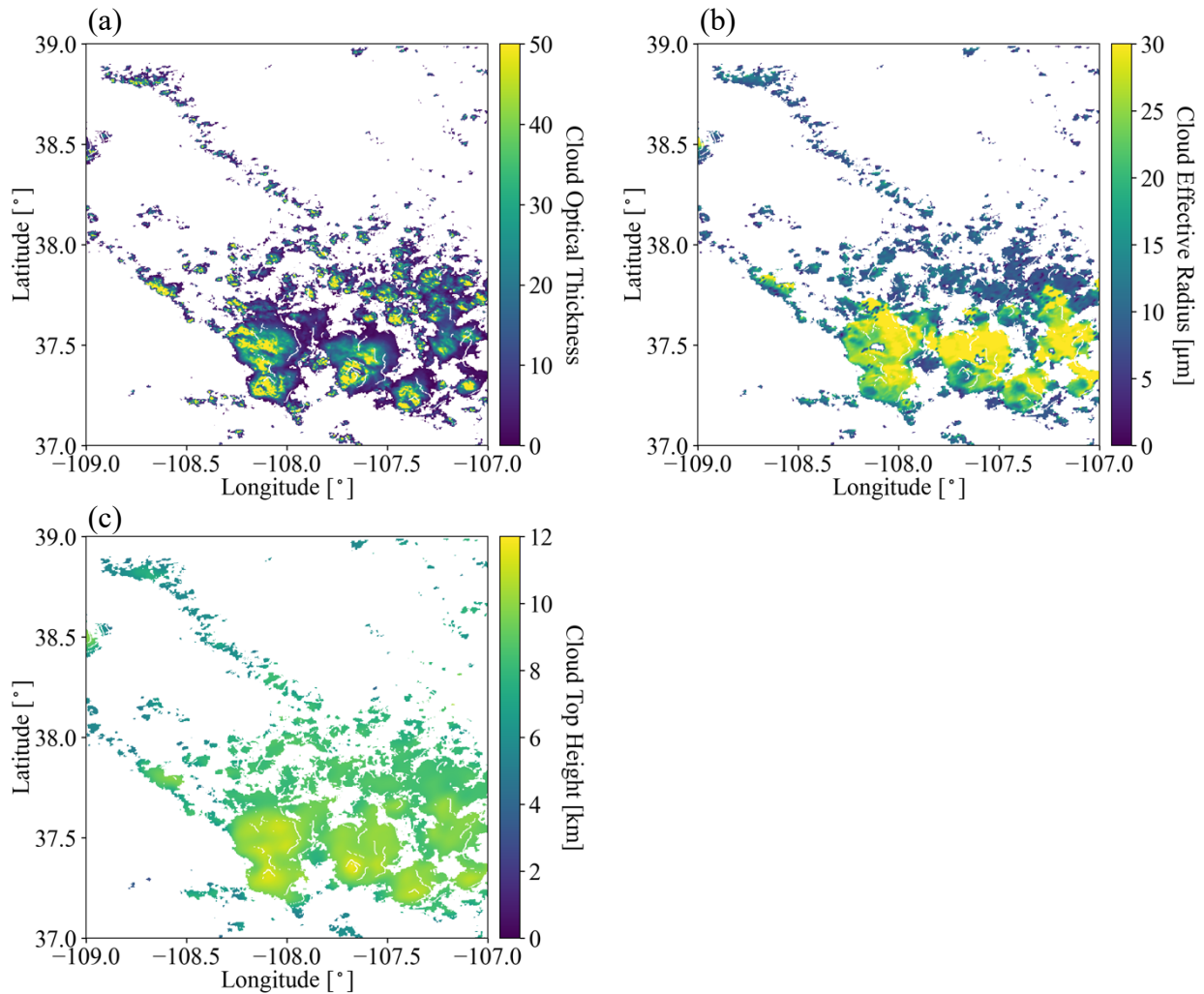
326 **2.2.2 Orbiting Carbon Observatory 2 (OCO-2)**

327 The OCO-2 satellite was inserted into NASA's A-Train constellation in 2014 and flies
328 about 6 minutes ahead of Aqua. OCO-2 provides the column-averaged carbon dioxide (CO₂)
329 dry-air mole fraction (XCO₂) through passive spectroscopy based on hyperspectral radiance
330 observations in three narrow wavelength regions, the Oxygen A-Band (~0.76 micron), the weak
331 CO₂ band (~1.60 micron), and the strong CO₂ band (~2.06 micron). As shown in the inset of Figure
332 2, it takes measurements in eight footprints across a narrow swath. Each of the footprints has a
333 size around 1-2 km, and the spectra for the three bands are provided by separate, co-registered
334 spectrometers (Crisp et al., 2015).

335 The OCO-2 data products of 1) Level 1B calibrated and geolocated science radiance
336 spectra (L1bScND), 2) standard Level 2 geolocated XCO₂ retrievals results (L2StdND), 3)
337 meteorological parameters interpolated from GMAO (L2MetND) at OCO-2 footprint location are
338 downloaded from NASA GES DISC (Goddard Earth Science Data Archive and Information
339 Services Center) data archive (https://oco2.gesdisc.eosdis.nasa.gov/data/OCO2_DATA). Since
340 MODIS on Aqua overflies a scene 6 minutes after OCO-2, the clouds move with the wind over
341 this time period. We therefore added a wind correction on top of the parallax-corrected cloud fields
342 obtained from MODIS (section 2.2.1). This was done with the 10 m wind speed data from
343 L2MetND (see Appendix D2). For the same scene as shown in Figure 2, Figure 3 shows (a) COT,
344 (b) CER, and (c) CTH, all corrected for both parallax and wind effects (these corrections are shown
345 in Figure A2 in Appendix D). The parallax and wind corrections are imperfect as certain
346 assumptions are involved. For example, they rely on the cloud top height from the MODIS cloud
347 product. In addition, they process the whole scene with one single sensor viewing geometry. To
348 minimize artifacts introduced by the assumptions, one can apply the simulation to a smaller region.

349

350



351

352

Figure 3. (a) Cloud optical thickness derived from MODIS L1B radiance at 650 nm by the two-stream approximation (Eq. A2), (b) cloud effective radius (units: μm), and (c) cloud top height (units: km) collocated from the MODIS L2 cloud product. The locations of the cloudy pixels were shifted to account for parallax and wind effects. The parallax correction ranged from near 0 for low clouds and 1 km for high clouds (10 km CTH). The wind correction was around 0.8 km, given the average wind speed of 2 m/s to the east.

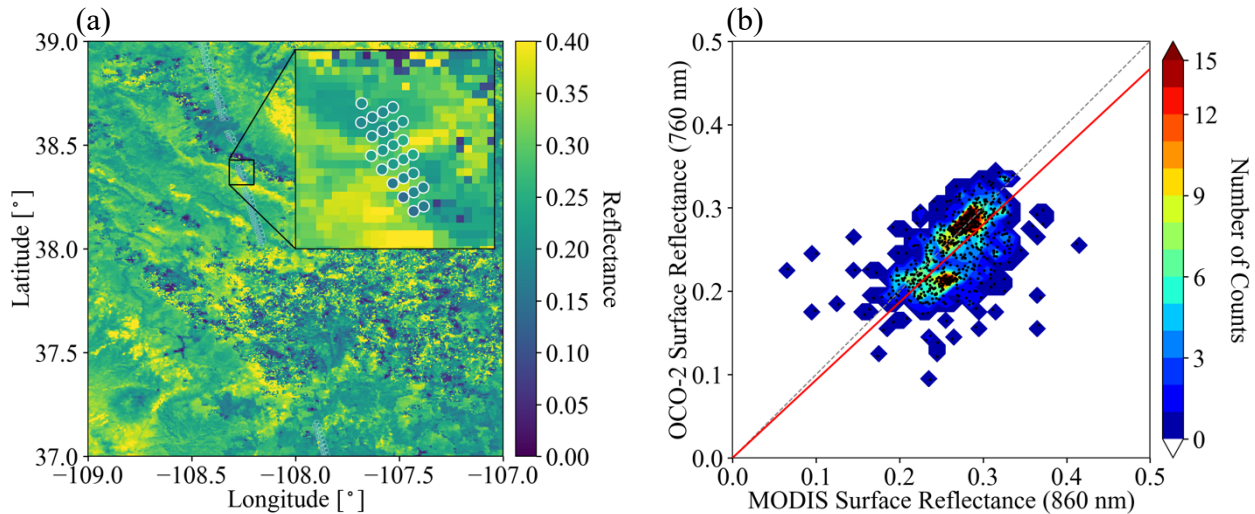
358

The OCO-2 data (L2StdND) themselves only provide sparse surface reflectance for the footprints that are clear, while EaR³T requires surface albedo for the whole domain. Therefore, we used MYD09A1 as a starting point. However, since MODIS does not have a channel in the Oxygen A-Band, MODIS band 2 (860 nm) was used as a proxy for the 760 nm OCO-2 channel as follows: we collocated the OCO-2 retrieved 760 nm surface reflectance R_{OCO} within the corresponding 860 nm MODIS MYD09A1 data R_{MOD} as shown in Figure 4a (same domain as Figures 2 and 3) and calculated a scaling factor assuming a linear relationship between R_{OCO} and R_{MOD} ($R_{OCO} = a \cdot R_{MOD}$).

365

366 Figure 4b shows R_{OCO} versus R_{MOD} for all cloud-free OCO-2 footprints. The red line shows a linear
 367 regression (derived scale factor $a=0.93$). Optionally, the OCO-2-scaled MODIS-derived surface
 368 reflectance fields can be replaced by the OCO-2 surface reflectance products for pixels where they
 369 are available. The scaled surface reflectance is then treated as surface albedo input to the RTM
 370 assuming a Lambertian surface.

371



372

373 **Figure 4.** (a) Surface reflectance from the OCO-2 L2 product in the Oxygen A-band (near 760 nm), overlaid on the
 374 surface reflectance from the MODIS MYD09 product at 860 nm. (b) OCO-2 surface reflectance at 760 nm
 375 versus MODIS surface reflectance at 860 nm, along with linear regression ($y=ax$) as indicated by the red
 376 line (slope $a=0.9337$).

377

378 2.2.3 Advanced Himawari Imager (AHI)

379 The Advanced Himawari Imager (AHI, used for App. 3) is a payload on Himawari-8, a
 380 geostationary satellite operated by the Meteorological Satellite Center (MSC) of the Japanese
 381 Meteorological Agency. The AHI provides 16 channels of spectral radiance measurements from
 382 the shortwave ($0.47\mu\text{m}$) to the infrared ($13.3\mu\text{m}$). During CAMP²Ex, the NASA in-field
 383 operational team closely collaborated with the team from MSC to provide AHI satellite imagery
 384 at the highest resolution over the Philippine Sea. From the AHI imagery, the cloud product
 385 generation system - Clouds from AVHRR Extended System (CLAVR-x), was used to generate
 386 cloud products from the AHI imagery (Heidinger et al., 2014). The cloud products from CLAVR-
 387 x include cloud optical thickness, cloud effective radius, and cloud top height at 2 (at nadir) to 5
 388 km spatial resolution. Since AHI provides continuous regional scans every 10 minutes the AHI
 389 cloud product has a temporal resolution of 10 minutes.

390

391 **2.2.4 Spectral Sunshine Pyranometer (SPN-S)**

392 The SPN-S is a prototype spectral version of the commercially available global-diffuse
393 SPN1 pyranometer (Wood et al., 2017; Norgren et al., 2022). The radiometer uses a 7-detector
394 design in combination with a fixed shadow mask that enables the simultaneous measurement of
395 both diffuse and global irradiances, from which the direct component of the global irradiance is
396 calculated via subtraction. The detector measures spectral irradiance from 350 to 1000 nm, and the
397 spectrum is sampled at 1 nm resolution with 1 Hz timing.

398 During the CAMP²Ex mission, the SPN-S was mounted to the top of the NASA P-3 aircraft
399 where it sampled downwelling solar irradiance. To ensure accurate measurements, pre- and post-
400 mission laboratory-based calibrations were completed using tungsten “FEL” lamps that are
401 traceable to a National Institute of Standards and Technology standard. Additionally, the direct
402 and global irradiances were corrected for deviations of the SPN-S sensor plane from horizontal
403 that are the result of changes in the aircraft’s pitch or roll. This attitude correction applied to the
404 irradiance data is a modified version of the method outlined in Long et al. (2010). However,
405 whereas Long et al. (2010) employ a “box” flight pattern to characterize the sensor offset angles,
406 in this study an aggregation of flight data containing aircraft heading changes under clear-sky
407 conditions are used as a substitute. The estimated uncertainty of the SPN-S system is 6 to 8%, with
408 4 to 6% uncertainty stemming from the radiometric lamp calibration process, and up to another 2%
409 resulting from insufficient knowledge of the sensor cosine response. The stability of the system
410 under operating conditions is 0.5%. A thorough description of the SPN-S and its calibration and
411 correction procedures is provided in Norgren et al. (2022). In this paper (App. 3) only the global
412 downwelling irradiance sampled by the 745 nm channel is used.

413

414 **2.2.5 Airborne All-Sky Camera (ASC)**

415 The All-Sky Camera (used for App. 4) is a commercially available camera (ALCOR
416 ALPHEA 6.0CW⁵) with fish-eye optics for hemispheric imaging. It has a Charge-Coupled Device
417 (CCD) detector that measures radiances in red, green, and blue channels. Radiometric and

⁵https://www.alcor-system.com/common/allSky/docs/ALPHEA_Camera%20ALL%20SKY%20CAMERA_Doc.pdf
last accessed on April 24, 2022.

418 geometric calibrations were performed at the Laboratory of Atmospheric and Space Physics at the
419 University of Colorado Boulder. The three-color channels are centered at 493, 555, and 626 nm
420 for blue, green, and red, respectively, with bandwidths of 50 – 100 nm. Only radiance data from
421 the red channel are used in this paper. The spatial resolution of the ASC depends on the altitude of
422 the aircraft and the viewing zenith angle. Across the hemispheric field of view of the camera, the
423 resolution of the field angle is approximately constant, at about 0.09° . At a flight level of 5 km,
424 this translates to a spatial resolution of 8 m at nadir. However, due to accuracy limitations of the
425 geometric calibration and the navigational data from Inertial Navigation System (INS), the nadir
426 geolocation accuracy could only be verified to within ± 50 m. During the CAMP²Ex flights, the
427 camera exposure time was set manually to minimize saturation of the detector. The standard image
428 frame rate is 1 Hz. The precision of the camera radiances is on the order of 1%, and the radiometric
429 accuracy is 6 – 7%.

430

431 **3. EaR³T Procedures**

432 In the previous section, we described the general workflow of EaR³T applications, along
433 with relevant data. In this section, we will focus on the specific implementation of the workflow
434 through the EaR³T software package. It is a toolbox for 3D-RT with modules for automatic input
435 data download and processing, generation of radiative and optical properties of surface,
436 atmospheric gases, clouds and aerosols, wrappers for 3D-RT solvers and output post-processing,
437 with the end goal to simulate radiances and irradiances along entire satellite orbits or aircraft flight
438 tracks. Unlike established radiative transfer packages such as libRadtran (Mayer and Kylling, 2005;
439 Emde et al., 2016), which provide extensive libraries of optical properties along with a selection
440 of solvers, EaR³T focuses on automated radiative transfer for two- or three-dimensional cloud,
441 aerosol, and surface input data, and therefore only comes with minimal options for optical
442 properties, and solvers. The initial release (version 0.1.0) is available at <https://github.com/hong-chen/er3t>.

444 We will now walk through the OCO-2 and MODIS simulator applications with the codes
445 `examples/01_oco2_rad-sim.py` (App. 1) and `examples/02_modis_rad-sim.py`
446 (App. 2). The data acquisition (first step in Figure 1) uses functions in `er3t/util`. App. 1 and
447 App. 2 use the functions in `er3t/util/modis.py` and `er3t/util/oco2.py` for
448 downloading the MODIS and OCO-2 data files from the respective NASA data archives and for

449 processing the data (e.g., geo-mapping, gridding etc.). The user supplies minimum input (date and
450 time, as well as latitudes and longitudes of the region of interest), which need to be specified in
451 `download_modis_https` and `download_oco2_https` (from `er3t/util`). For
452 example, for App. 1 and App. 2, the only user inputs are the date and time and the region of interest
453 – in this case September 2, 2019, with the westernmost, easternmost, southernmost, and
454 northernmost longitudes and latitudes of 109°W, 107°W, 37°N, and 39°N. In order for EaR³T to
455 access any data archives such as NASA Earthdata, the user needs to create an account with them
456 and store the credentials locally (detailed instructions are provided separately along with the EaR³T
457 distribution).

458 After the data acquisition step, the satellite data are fed into the pre-processing step for 1)
459 atmospheric gases (`er3t/pre/atm`), 2) clouds (`er3t/pre/cld`), 3) surface
460 (`er3t/pre/sfc`) as shown in Figure 1. In the default configuration of the App. 1, the standard
461 US atmosphere (Anderson et al., 1986; included in the EaR³T repository) is used within `atm`.
462 EaR³T supports the input of user-specified atmospheric profiles, e.g., atmospheric profiles from
463 reanalysis data for App. 2 as described in Schmidt et al. (2022), by making changes in
464 `atm_atmmod` (from `er3t/pre/atm`). Subsequently, molecular scattering coefficients are
465 calculated by `cal_mol_ext` (from `er3t/util`), and absorption coefficients for atmospheric
466 gases are generated by (`er3t/pre/abs`). At the current development stage, two options are
467 available:

468 1. Line-by-line (used by App. 1): The repository includes a sample file of absorption coefficient
469 profiles for a subset of wavelengths within OCO-2’s Oxygen A-Band channel, corresponding
470 to a range of atmospheric transmittance values from low (opaque) to high (so-
471 called “continuum” wavelength). They were generated by an external code (Schmidt et al.,
472 2022) based on OCO-2’s line-by-line absorption coefficient database (ABSCO, Payne et al.,
473 2020). For each OCO-2 spectrometer wavelength within a given channel, hundreds of
474 individual absorption coefficient profiles at the native resolution of ABSCO need to be
475 considered across the instrument line shape (ILS, also known as the slit function) of the
476 spectrometer. The ILS, as well as the incident solar irradiance, are also included in the file.
477 In subsequent steps, EaR³T performs RT calculations at the native spectral resolution of
478 ABSCO, but then combines the output by convolving with the ILS and outputs OCO-2
479 radiances or reflectances at the subset of wavelengths. For probabilistic (Monte Carlo) RT

480 solvers such as MCARaTS, the number of photons can be kept relatively low (e.g., 10^6
481 photons), and can be adjusted according to the values of the ILS at a particular ABSCO
482 wavelength. Any uncertainty at the ABSCO spectral resolution due to photon noise is greatly
483 reduced by convolving with the ILS for the final output.

484 2. Correlated-k (used by App. 2): This approach (Mlawer et al., 1997) is appropriate for
485 instruments such as MODIS with much coarser spectral resolution than OCO-2, as well as
486 for broadband calculations. In contrast to the line-by-line approach, RT calculations are not
487 performed at the native resolution of the absorption database, but at Gaussian quadrature
488 points (called “g’s”) that represent the full range of sorted absorption coefficients, and then
489 combined using Gaussian quadrature weights. The repository includes an absorption
490 database from Coddington et al. (2008), developed specifically for a radiometer with
491 moderate spectral resolution on the basis of HITRAN (high-resolution transmission
492 molecular absorption database) 2004 (Rothman et al., 2005). It was created for the ILS of
493 the airborne Solar Spectral Flux Radiometer (SSFR, Pilewskie et al., 2003), but is applied to
494 MODIS here, which has a moderate spectral resolution of 8-12 nm with 20-50 nm
495 bandwidths. It uses 16 absorption coefficient bins (g’s) per target wavelength (this could
496 either be an individual SSFR or a MODIS channel), which are calculated by EaR³T with the
497 Coddington et al. (2008) database using the mixing ratios of atmospheric gases in the
498 previously ingested profile. In future implementations, the code will be updated to enable
499 flexible ILS and broadband calculations.

500 The `er3t/pre/cld` module calculates extinction, thermodynamic phase, and effective
501 droplet radius of clouds from the input data. The `er3t/pre/pha` module creates the required
502 single scattering albedo and scattering phase function. The default is a Henyey-Greenstein phase
503 function with a fixed asymmetry parameter of 0.85. Along with the current distribution (v0.1.0) of
504 EaR³T, the Mie phase functions based on thermodynamic phase, effective droplet radius, and
505 wavelength are supported. In this study, App. 1 and App. 2 use Mie phase functions calculated
506 from Legendre polynomial coefficients (originally distributed along with libRadtran) based on the
507 wavelength and cloud droplet effective radius. In the future, EaR³T will include stand-alone phase
508 functions, which can be chosen on the basis of droplet size distributions in addition to effective
509 radius. It is also possible to include aerosols in a similar fashion as clouds. This is done with the

510 `er3t/pre/aer` module. In the case of aerosols, spectral single scattering albedo and asymmetry
511 parameter are required as inputs in addition to the extinction fields.

512 After the optical properties are calculated, they are passed into the 3D-RT step
513 (`er3t/rtm/mca`). In addition to MCARaTS, planned solvers for the future include MYSTIC
514 (Monte Carlo code for the physically correct tracing of photons in cloudy atmospheres, Mayer,
515 2009) and SHDOM (Spherical Harmonic Discrete Ordinate Method, Evans, 1998; Pincus and
516 Evans, 2009). This step performs the setup of RT solver-specified input parameters and data files,
517 distributing runs over multiple Central Processing Units (CPUs), and post-processing RT output
518 files into a single, user-friendly HDF5 file. For example, when radiance is specified as output
519 (default in App. 1 and App. 2), key information such as the radiance field and its standard deviation
520 are stored in the final HDF5 file (details see Table 1).

521 While the EaR³T repository comes with various applications such as App. 1 and App. 2,
522 described above, the functions used by these master or ‘wrapper’ programs can be organized in
523 different ways, where the existing applications serve as templates for a quick start when developing
524 new applications. The functions used by the master code pass information through the various
525 steps as Python objects. For example, in `examples/01_oco2_rad-sim.py`, the downloaded
526 and processed satellite data are stored into the `sat` object. Later, the `sat` object is passed into an
527 EaR³T function to create the `cld` object that contains cloud optical properties. Similarly, EaR³T
528 provides functions to create the `atm`, and `sfc` objects with optical properties for atmospheric
529 gases and the surface. These objects (`atm`, `cld`, `sfc`) are in turn passed on to solver-specific
530 modules for performing RT calculations. The user can choose to save the data of the intermediate
531 objects into Python pickle files after the first run. In this way, multiple calls with identical input
532 can re-use existing data, which accelerates the processing time of EaR³T. Unless the user specifies
533 the `overwrite` keyword argument in the object call to reject saving pickle files, these shortcuts
534 save significant time. Moreover, EaR³T is capable of distributing simulations over multiple CPUs
535 to accelerate the calculations, which is useful for potential future application of later EaR³T or
536 EaR³T-like codes in operational or large-scale data processing.

537 In the following sections, we discuss results obtained from EaR³T, starting with those from
538 `examples/01_oco2_rad-sim.py` and `examples/02_modis_rad-sim.py` (section
539 4), `examples/03_spns_flux-sim.py` (section 5), and concluding with

540 `examples/04_cam_nadir_rad-sim.py` (section 6). The detailed RT setup for the
541 applications is provided Table A1 in Appendix A.

542

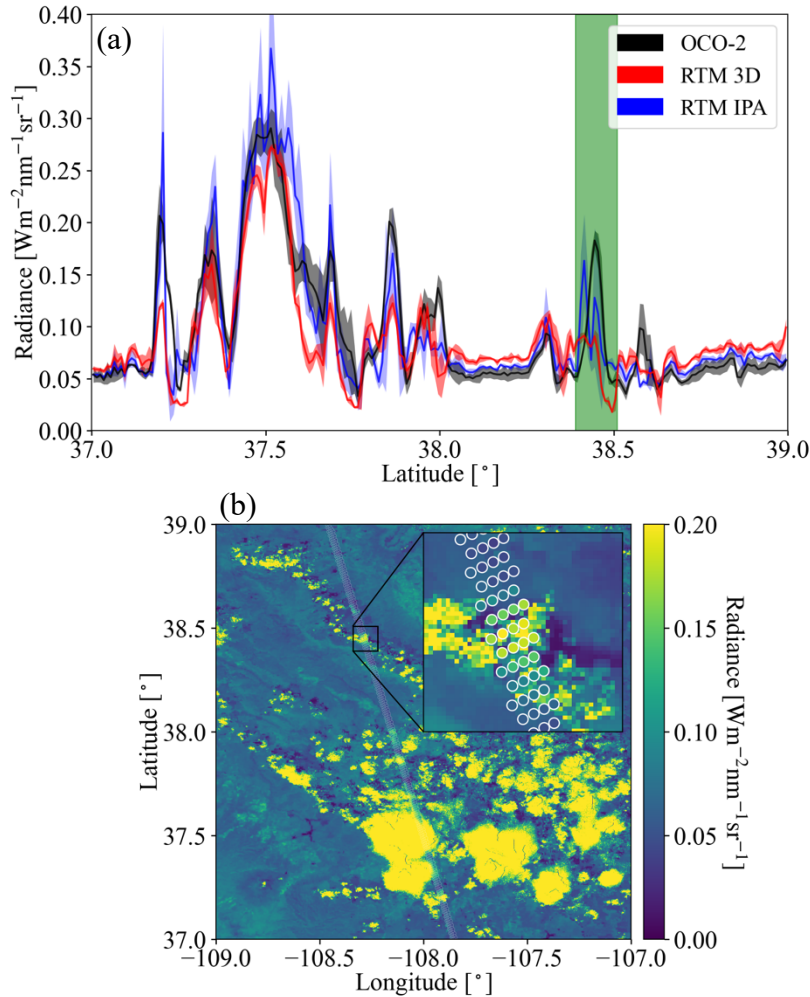
543 **4. EaR³T as a 3D Satellite Radiance Simulator**

544 This section demonstrates the automated 3D radiance simulation for satellite instruments
545 by EaR³T for OCO-2 and MODIS measured radiance based on publicly available MODIS retrieval
546 products. The OCO-2 application is an example of radiance consistency between two distinct
547 satellite instruments where the measurements of one (here, OCO-2) are compared with the
548 simulations based on data products from the other (here, MODIS). The MODIS application, on
549 the other hand, is an example of radiance self-consistency. We will show how inconsistencies can
550 be used for detecting cloud and surface property retrieval biases.

551 **4.1 OCO-2 (App. 1)**

552 The OCO-2 radiance measurements at 768.52 nm for our sample scene in the context of
553 MODIS imagery were shown in Figure 2. For that track segment, Figure 5a shows the simulated
554 radiance along with the measurements as a function of latitude. The radiance was averaged over
555 every 0.01° latitude window from 37° N to 39° N (the standard deviation within the bin indicated
556 by the shaded color). In clear-sky regions (e.g., around 38.2° N), the simulations (red) are
557 systematically higher than the measurements (black), even though the footprint-level OCO-2
558 retrieval was used to scale the MYD09 surface reflectance field as described in section 2.2.2
559 (Figure 4). This is because, unlike the MYD09 algorithm which relies on multiple overpasses and
560 multiple-days for cloud-clearing, the OCO-2 retrieval is done for any clear footprint. Clouds in the
561 vicinity lead to enhanced diffuse illumination that is erroneously attributed to the surface
562 reflectance itself. The EaR³T IPA calculations of the clear-sky pixels (blue) essentially reverse the
563 3D effect and therefore match the observations better. The 3D calculations enhance the reflectance
564 through the very same 3D cloud effects that led to the enhanced surface illumination in the first
565 place. It is possible to correct this effect by down-scaling the surface reflectance according to the
566 ratio between clear-sky 3D and IPA calculations, but this process is currently not automated.

567



568

569

570 **Figure 5. (a)** Latitudinally averaged (0.01° spacing) radiance calculations from EaR³T (red: 3D, blue: IPA) and OCO-
 571 2 measured radiance at 768.52 nm (black) The green shaded area indicates the inset shown in (b). **(b)** The
 572 same as Figure 2 except OCO-2 measured radiance overlaid on IPA radiance simulations at 768.52 nm. The
 573 solar zenith angle (SZA) for the radiance simulation case is 33.57° .

574

575 In the cloudy locations, the IPA calculations match the OCO-2 observations on a footprint-
 576 by-footprint level (see Figure 5b), demonstrating that wind and parallax corrections were
 577 performed successfully. Of course, there is not always a perfect agreement because of
 578 morphological changes in the cloud field over the course of six minutes. It is, however, apparent
 579 that the 3D calculations agree to a much lesser extent with the observations than the IPA
 580 calculations. Just like the mismatch for the clear-sky pixels indicates a bias in the input surface
 581 reflectance, the bias here means that the input cloud properties (most importantly COT) are
 582 inaccurate. For most of the reflectance peaks, the 3D simulations are too low, which means that

583 the input COT is biased low. This is due to 3D cloud effects on the MODIS-based cloud retrieval.
584 Since they are done with IPA, any net horizontal photon transport is not considered, which leads
585 to an apparent surface brightening as noted above, at the expense of the cloud brightness. As a
586 result, the COT from darker clouds is significantly underestimated. This commonly known
587 problem (Barker and Liu, 1995), with several aspects discussed in the subsequent EaR³T
588 applications, can be identified by radiance consistency checks such as the one shown in Figure 5,
589 and mitigated by novel types of cloud retrievals that do take horizontal photon transport into
590 account (section 6).

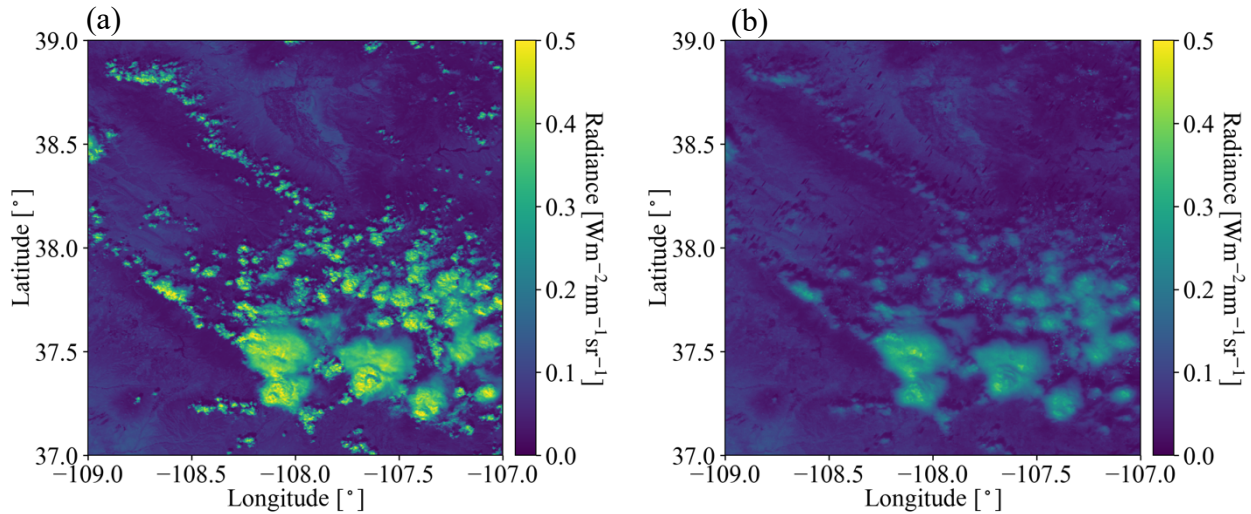
591

592 **4.2 MODIS (App. 2)**

593 To go beyond the OCO-2 track and understand the bias between simulated and observed
594 radiances from a domain perspective, we now consider the radiance simulations for the MODIS
595 650 nm channel. The setup is exactly the same as for the OCO-2 simulations, except that 1) the
596 viewing zenith angle is set to the average viewing zenith angle of MODIS within the shown domain
597 (instead of OCO-2), and 2) the surface reflectances from MYD09 are used directly, this time from
598 the 650 nm channel without rescaling. Figure 6a shows the MODIS measured radiance field, while
599 Figure 6b shows the EaR³T 3D simulations. Visually, the clouds from the EaR³T simulation are
600 generally darker than the observed clouds, which is in line with our aforementioned explanation
601 of net horizontal photon transport. They are also blurrier because radiative smoothing (Marshak et
602 al., 1995) propagates into the retrieved COT fields, which are subsequently used as input to EaR³T.
603 To look at darkening and smoothing effects more quantitatively, Figure 7 shows a heatmap plot of
604 simulated radiance versus observed radiance. It shows that the radiance for cloud-covered pixels
605 (labeled “cloudy”) from EaR³T are mostly low-biased while good agreement between simulations
606 and observations was achieved for clear-sky radiance (labeled “clear-sky”). The good agreement
607 over clear-sky regions is expected. As mentioned above, we use MYD09 as surface reflectance
608 input, which in contrast to the OCO-2 surface reflectance product is appropriately cloud-screened
609 and therefore does not have a reflectance high bias. There is, of course, a reflectance enhancement
610 in the vicinity of clouds, but that is captured by the EaR³T calculations. The fact that the
611 calculations agree with the observations even for clear-sky pixels in the vicinity of clouds, shows
612 that the concept of radiance consistency works to ensure correct satellite retrievals even in the
613 presence of clouds. It also corroborates our observation from section 4.1 that COT_{IPA} is low biased.

614 Since the MODIS reflectance is *not* self-consistent with respect to COT_{IPA} as shown for the *cloudy*
 615 pixels in Figure 7, we can identify a bias in the cloud properties even without knowing the ground
 616 truth of COT. On the other hand, successful closure in radiance (self-consistency) would provide
 617 an indication that the input fields including COT are accurate, although it is certainly a weaker
 618 metric than direct verification of the retrievals through aircraft satellite retrieval validation with
 619 in-situ instruments.

620



621

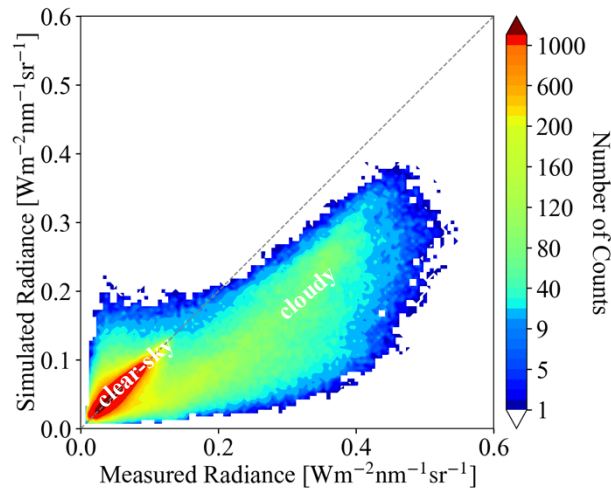
622 **Figure 6. (a)** MODIS measured radiance in channel 1 (650 nm). **(b)** Simulated 3D radiance at 650 nm from EaR³T.

623

The solar zenith angle for the radiance simulation case is 34.42°.

624

625



626

627 **Figure 7.** Heatmap plot of EaR³T simulated 3D radiance vs. MODIS measured radiance at 650 nm.

628

629 Summarizing the two satellite radiance simulator applications, one can say that EaR³T
630 enables a radiance consistency check for inhomogeneous cloud scenes. We demonstrated that a
631 lack of simulation-observation consistency (MODIS versus OCO-2) and self-consistency (MODIS
632 versus MODIS) can be traced back to biased surface reflectance or cloud fields in the simulator
633 input. This can become a diagnostic tool for the quality of retrieval products from future or current
634 missions, even when the ground truth is not known. It should be pointed out that the vertical extent
635 of the clouds affects the simulated radiance – the larger the vertical extent, the larger the 3D effects
636 (more horizontal photon transport). Since we make the assumption of a cloud geometric thickness
637 of 1 km if no thickness information is provided, the simulated radiance at the satellite sensor level
638 is valid for that proxy cloud only. For deeper clouds, the simulated radiance would be even lower.
639 Either way, the comparison with the actual radiance measurements will reveal a lack of closure.
640 Additionally, although the clouds introduce the lion’s share of the 3D bias that is identified by the
641 radiance consistency check, additional discrepancies can be introduced in different ways. For
642 example, the topography (mountainous region in Colorado) is not considered by MCARaTS (it is
643 considered by MYSTIC, but this solver has not been implemented yet).

644 For technical reference: The MODIS simulation (domain size of [Nx=1188, Ny=1188])
645 took about one hour on a Linux workstation with 12 CPUs for three 3D RT runs with 10⁸ photons
646 each. With a slightly modified setup and parallelization, the automation can be easily applied for
647 entire satellite orbits, although more research is required to optimize the computation speed
648 depending on the desired output accuracy.

649

650 **5. EaR³T as 3D Aircraft Irradiance Simulator (App. 3)**

651 In contrast to the previous applications that focused on satellite remote sensing, we will
652 now be applying EaR³T to quantify 3D cloud retrieval biases through direct, systematic validation
653 of imagery-derived *irradiances* against aircraft measurements, instead of using the indirect path
654 of radiance consistency in section 4. Previous studies (e.g., Schmidt et al., 2007; Kindel et al.,
655 2010) conducted radiative closure between remote sensing derived and measured irradiance using
656 isolated flight legs as case studies. Here, with the efficiency afforded by the automated nature of
657 EaR³T, we are able to conduct radiative closure of irradiance through a statistical approach that
658 employs campaign-scale amounts of measurement data. Specifically, we used EaR³T to perform
659 large-scale downwelling irradiance simulations at 745 nm based on geostationary cloud retrievals

660 from AHI for the CAMP²Ex campaign, and directly compare these simulations to the SPN-S
661 measured irradiances onboard the P-3 aircraft. This is done for all below-cloud legs from the entire
662 campaign with the aim to assess the degree to which satellite-derived near-surface irradiances
663 reproduce the true conditions below clouds.

664 The irradiance simulation process is similar to the previously described radiance simulation
665 in section 4, with only a few modifications. First, we used cloud optical properties from the AHI
666 cloud product (COT, CER and CTH) as direct inputs into EaR³T. Secondly, we used a constant
667 ocean surface reflectance value of 0.03. Such simplification in surface albedo is made under the
668 assumption that 1) the ocean surface is calm with no whitecaps, and that 2) the Lambertian
669 bidirectional reflectance distribution function (BRDF) is sufficient (instead of directionally
670 dependent BRDF) to represent surface albedo for the irradiance calculation. Since the ocean
671 surface albedo can greatly differ from 0.03 when the Sun is extremely low (Li et al., 2006), we
672 excluded data under low-Sun conditions where the SZA is greater than 45°. Lastly, since EaR³T
673 can only perform 3D simulations for a domain at a single specified solar geometry, we divided
674 each CAMP²Ex research flight into small flight track segments where each segment contains 6
675 minutes of flight time. The size and shape of the flight track segments can vary significantly due
676 to the aircraft maneuvers, aircraft direction, aircraft speed, etc. For each flight track segment,
677 EaR³T performs irradiance simulations for a domain that extends half a degree at an averaged solar
678 zenith angle. In contrast to the radiance simulation output, which is two-dimensional at a specified
679 altitude and sensor geometry, the irradiance simulation output is three dimensional. In addition to
680 x (longitude) and y (latitude) vectors, it has a vertical dimension along z (altitude). From the
681 simulated three-dimensional irradiance field, the irradiance for the flight track segment is linearly
682 interpolated to the x-y-z location (longitude, latitude, and altitude) of the aircraft. EaR³T
683 automatically sub-divides the flight track into tiles encompassing track segments, and extracts the
684 necessary information from the aircraft navigational data. Based on the aircraft time and position,
685 EaR³T downloads the AHI cloud product that is closest in time and space to the domain containing
686 the flight track segment.

687 Figure 8 shows the simulated irradiance for a sample flight track below clouds on 20
688 September, 2019. Figure 8a shows the flight track overlaid on AHI imagery. Figure 8b shows 3D
689 (in red) and IPA (in blue) downwelling irradiance simulations for the highlighted flight track in
690 Figure 8a, as well as measurements by the SPN-S (in black). Since the 3D and IPA simulations

691 are performed separately at discrete solar and sensor geometries for each flight track segment based
692 on potentially changing cloud fields from one geostationary satellite image to the next,
693 discontinuities in the calculations (indicated by gray dashed lines) are expected. The diffuse
694 irradiance (downwelling and upwelling) can also be simulated and compared with radiometer
695 measurements (not shown here). Since the irradiance was simulated/measured below clouds, high
696 values of downwelling irradiance indicate thin-cloud or cloud-free regions while low values of
697 downwelling irradiance indicate thick-cloud regions. The simulations successfully captured this
698 general behavior – clouds thickened from west to east until around 121.25° E, and thinned
699 eastwards. However, the fine-scale variabilities in irradiance were not captured by the simulations
700 due to the coarse resolution of COT in the AHI cloud product (3-5 km). Additionally, the
701 simulations also missed the clear-sky regions in the very east and west of the flight track as
702 indicated by high downwelling irradiance values measured by SPN-S. This is probably also due to
703 the coarse resolution of the AHI COT product where small cloud gaps are not represented. Large
704 discrepancies between simulations and observations occur in the mid-section of the flight track
705 where clouds are present (e.g., longitude range from 121.15° to 121.3°). Although the 3D
706 calculations differ somewhat from the IPA results, they are both biased high, likely because the
707 input COT (the IPA-retrieved AHI product) is biased low. This bias is caused by the same
708 mechanism that was discussed earlier in the MODIS examples (section 4.2). This begs the question
709 whether this is true for the entire field mission. To answer the question, we performed a *systematic*
710 comparison of the cloud transmittance for *all* available below-cloud flight tracks from CAMP²Ex,
711 using EaR³T's automated processing pipeline. The output of this pipeline is visualized in time-
712 synchronized flight videos (Chen et al., 2022), which show the simulations and observations along
713 all flight legs point by point. These videos give a glimpse of the general cloud environment during
714 the field campaign from the geostationary satellite perspective.

715

716

717

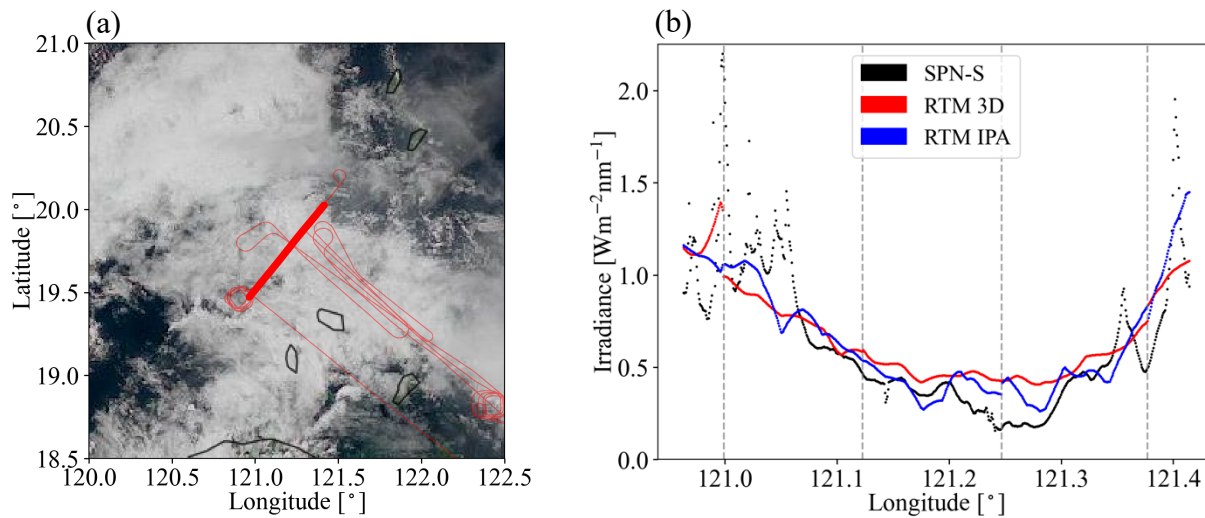
718

719

720

721

722



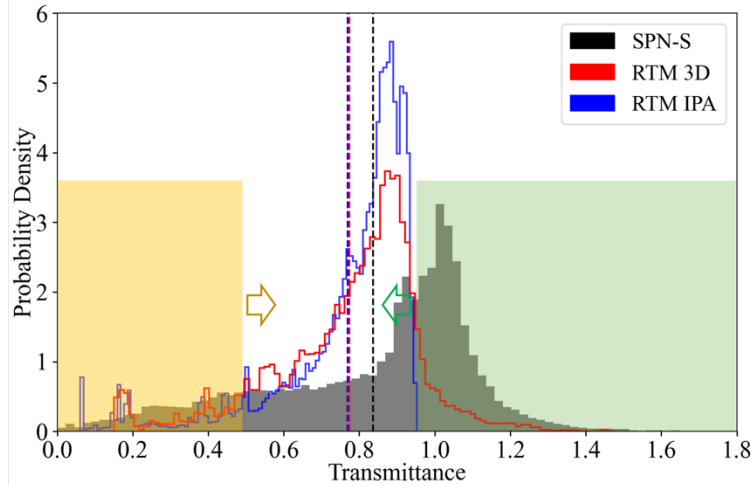
723

724 **Figure 8. (a)** Flight track overlay HIMAWARI AHI RGB imagery over the Philippine Sea on 20 September, 2019.725 The thin line shows the entire flight track within the domain. The thick line highlights the specific leg
726 analyzed in (b). **(b)** Measured downwelling irradiance from SPN-S at 745 nm and calculated 3D and IPA
727 irradiance from EaR³T for the highlighted flight track in (a).

728

729 For this comparison, we use transmittance instead of irradiance. The transmittance is
730 calculated by dividing the downwelling irradiance below clouds (F_{\downarrow}^{bottom}) by the downwelling
731 irradiance at the top of the atmosphere extracted from the Kurucz solar spectra (F_{\downarrow}^{TOA} ; Kurucz,
732 1992) at incident solar zenith angle (SZA), where $Transmittance =$ 733 $F_{\downarrow}^{bottom} / (F_{\downarrow}^{TOA} \cdot \cos(SZA))$. Thus the transmittance has less diurnal dependence than the734 irradiance. Figure 9 shows the histograms of the simulated and measured cloud transmittance from
735 all below-cloud legs. The average values are indicated by dashed lines. Although the averaged
736 values of IPA and 3D transmittance are close, their distributions are different. Only the 3D
737 calculations and the measured transmittance reach values beyond 1. This occurs in clear-sky
738 regions in the vicinity of clouds that receive photons scattered by the clouds as previously
739 discussed for the OCO-2 application.

740



741
 742 **Figure 9.** Histogram of measured transmittance from SPN-S at 745 nm (black) and calculated 3D (red) and IPA (blue)
 743 transmittance from EaR³T for all the below-cloud flight tracks during CAMP²Ex in 2019. The mean values
 744 are indicated by dashed lines. The yellow (green) shaded area represents the relatively low (high)
 745 transmittance region where the probability density of the observed transmittance (black) is greater than the
 746 calculations.

747
 748 Both the distribution and the mean value of the simulations are different from the
 749 observations – the simulation histograms peak at around 0.9 while the observation histogram peaks
 750 at around 1. The histograms indicate that the RT simulations miss most of the clear-sky conditions
 751 because of the coarse resolution of the AHI cloud product. If clouds underfill a pixel, AHI
 752 interprets the pixel as cloudy in most cases. This leads to an underestimation of clear-sky regions
 753 since cumulus and high cirrus were ubiquitous during CAMP²Ex. The area on the left (highlighted
 754 in yellow) has low cloud transmittance associated with thick clouds. In this range, the histograms
 755 of the calculations are generally below the observations, and the PDF of the calculations is offset
 756 to the right (indicated by the yellow arrow). This means that the transmittance is overestimated by
 757 both IPA and 3D RT, and thus that the COT of thick clouds is underestimated, consistent with
 758 what we found before (Figure 8b). The high-transmittance end (highlighted in green) is associated
 759 with clear-sky and thin clouds. Here, the peak of the PDF is shifted to the left (green arrow), and
 760 the calculations are biased low. This is caused by a combination of 1) the overestimation in COT
 761 of thin clouds due a 3D bias in the AHI IPA retrieval, 2) the aforementioned resolution effect that
 762 underestimates the occurrence of clear-sky regions (or overestimation in cloud fraction), and 3)
 763 net horizontal photon transport from clouds into clear-sky pixels. Overall, the calculations
 764 underestimate the true transmittance by 10%. This might seem to contradict Figure 7, where the

765 calculated reflected radiance was biased low due to the *underestimation* of COT in the heritage
766 retrievals, which would correspond to an *overestimation* of the radiation transmitted by clouds.
767 This effect is indeed apparent in the yellow-shaded area of Figure 9 (high COTs), but the means
768 (dashed lines) show exactly the opposite. To understand that, one has to consider that the histogram
769 depicts all-sky conditions, which include both cloudy and clear pixels. In this case, the direction
770 of the overall (all-sky) bias follows the direction of the thin-cloud/clear bias, rather than the
771 direction of the thick cloud bias. For different study regions of the globe with different cloud
772 fractions, cloud size distributions, and possibly different imager resolutions, the direction and
773 magnitude of the bias might be very different.

774 Summarizing, this application demonstrates that the EaR³T’s automation feature allows
775 systematic simulation-to-observation comparisons. If aircraft observations are available, then
776 closure between satellite-derived irradiance and suborbital measurements is a more powerful
777 verification of satellite cloud retrieval products than the radiance consistency from the earlier
778 stand-alone satellite applications. Even more powerful is the new approach to process the data
779 from an entire field mission for assessing the quality of cloud products in a region of interest (in
780 this case, the CAMP²Ex area of operation).

781

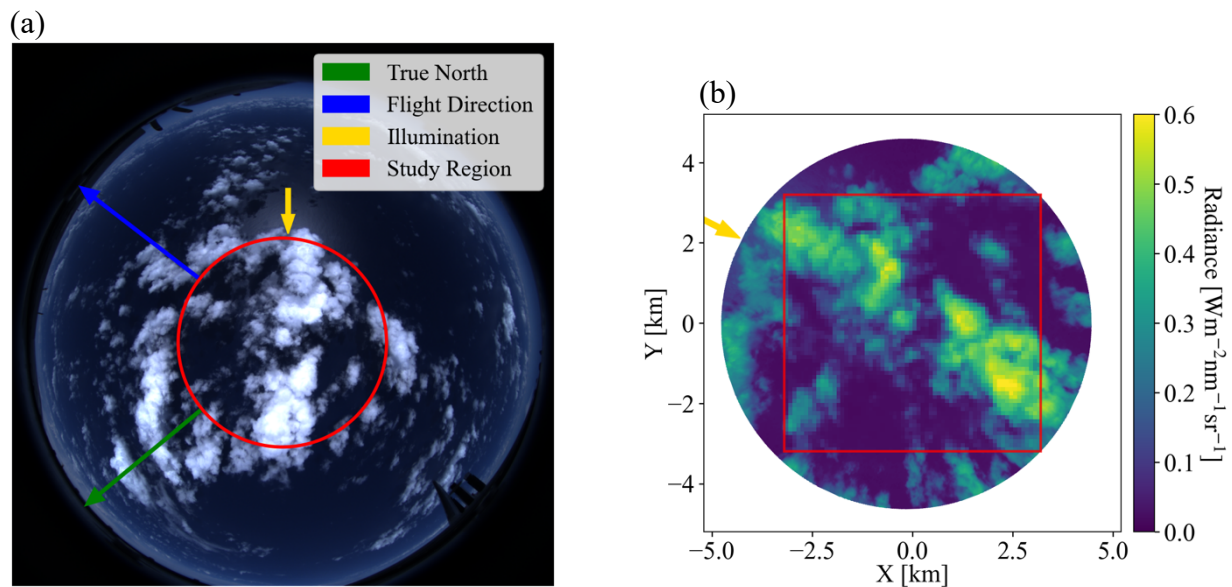
782 **6. EaR³T for Mitigating 3D Cloud Retrieval Biases (App. 4)**

783 In this section, we will use high-resolution imagery from a radiometrically calibrated
784 all-sky camera flown during the CAMP²Ex to isolate the 3D bias (sometimes referred to as IPA
785 bias) and explore its mitigation with a newly developed CNN cloud retrieval framework (Nataraja
786 et al., 2022). The CNN, unlike IPA, takes pixel-to-pixel net horizontal photon transport into
787 account. It exploits the spatial context of pixels in cloud radiance imagery, and extracts a higher-
788 dimensional, multi-scale representation of the radiance to retrieve COT fields as the output. It does
789 so by learning on “training data”, which in this case was input radiance and COT pairs synthetically
790 generated by EaR³T using LES data from the Sulu Sea. The best CNN model, trained on different
791 coarsened resolutions of the data pairs, is included within the EaR³T repository. For App. 4, this
792 CNN is applied to real imagery data for the first time, which in our case are near-nadir observations
793 by the all-sky camera (section 2.2.5) that flew in CAMP²Ex.

794 The CNN model was trained at a single (fixed) sun-sensor geometry (solar zenith angle,
795 SZA=29.2°; solar azimuth angle, SAA=323.8°, viewing zenith angle, VZA=0°), at a spatial

796 resolution of 100 m. We therefore chose a camera scene with a matching SZA (28.9°), and rotated
 797 the radiance imagery to match SAA= 323.8° , and subsequently gridded the 8-12 m native
 798 resolution camera data to 100 m. Figure 10a shows the RGB imagery captured by the all-sky
 799 camera over the Philippine Sea at 02:10:06 UTC on 5 October 2019. The Sun is located at the
 800 southeast (as indicated by the yellow arrow) and can be easily identified from the sun glint. Note
 801 that this image has not yet been geolocated; it is depicted as acquired in the aircraft reference frame.
 802 Figure 10b shows the rotated scene of the red channel radiance for the region encircled in yellow
 803 in Figure 10a. The sun (as indicated by the yellow arrow) is now at SAA= 323.8° . The selected
 804 study region is indicated by the red rectangle in Figure 10b ($6.4 \times 6.4 \text{ km}^2$), where the raw radiance
 805 of the camera is gridded at 100 m resolution to match the spatial resolution of the training dataset
 806 of the CNN.

807
 808



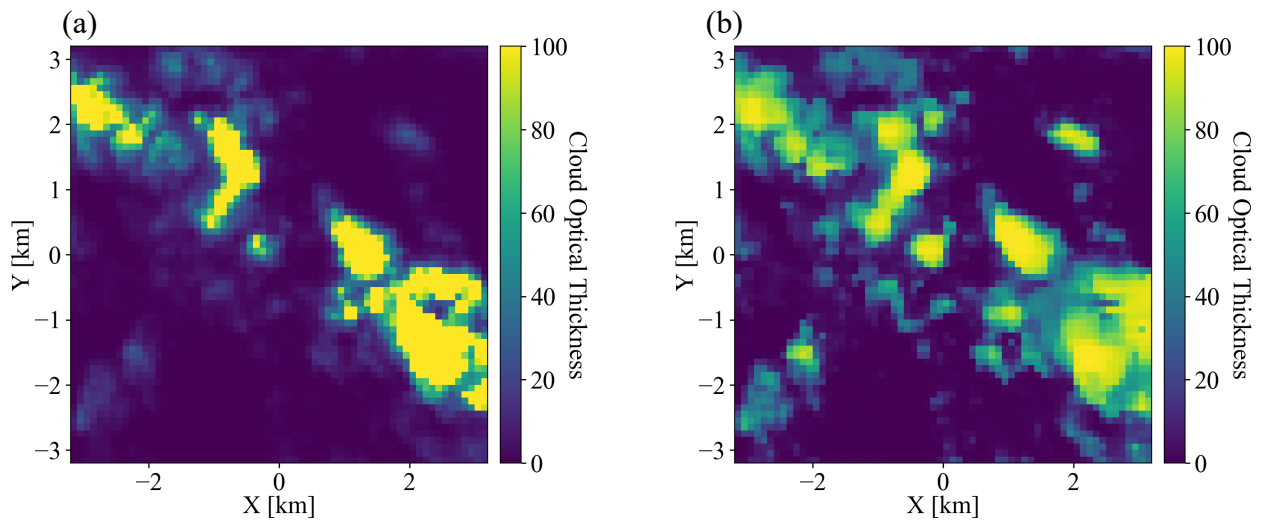
809
 810 **Figure 10.** (a) RGB imagery of nadir-viewing all-sky camera deployed during CAMP²Ex for a cloud scene centered
 811 at [123.392°E , 15.2744°N] over the Philippine Sea at 02:10:06 UTC on 5 October, 2019. The arrows
 812 indicate the true north (green), flight direction (blue), and illumination (where the sunlight comes from,
 813 yellow). (b) Red channel radiance measured by the camera for the circular area indicated by the red circle
 814 in (a). Red squared region shows gridded radiance with a pixel size of 64×64 and spatial resolution of 100
 815 m.

816

817 From the radiance field, we used both the traditional IPA (based on the two-stream
 818 approximation) and the new CNN to retrieve COT fields. Figure 11 shows the COT_{IPA} and COT_{CNN}

819 fields, which are visually quite different. For relatively thin clouds (e.g., at around $\{2, 1.8\}$), the
820 CNN tends to retrieve larger COT values than COT_{IPA} . Also, it returns more spatial structure than
821 the IPA (e.g., around $\{2, -1\}$). To assess how either retrieval performs, we now apply the radiance
822 self-consistency approach introduced with MODIS data in section 4.2. Using both the IPA and the
823 CNN retrieval as input, we had EaR³T calculate the (synthetic) radiance that the camera should
824 have observed if the retrieval were accurate. The clouds are assumed to be located at 1-2 km. Such
825 an assumption is inferred from low-level aircraft observations of clouds on the same day. These
826 radiance fields are shown in Figure 12a and 12b, and can be compared to Figure 12c. Seven edge
827 pixels have been removed from the original domain because the CNN performs poorly at edge
828 pixels, and because the 3D calculations use periodic boundary conditions.

829



830

831 **Figure 11.** Cloud optical thickness for the gridded radiance in Figure 10b (a) estimated by IPA and (b) predicted by
832 CNN.

833

834

835

836

837

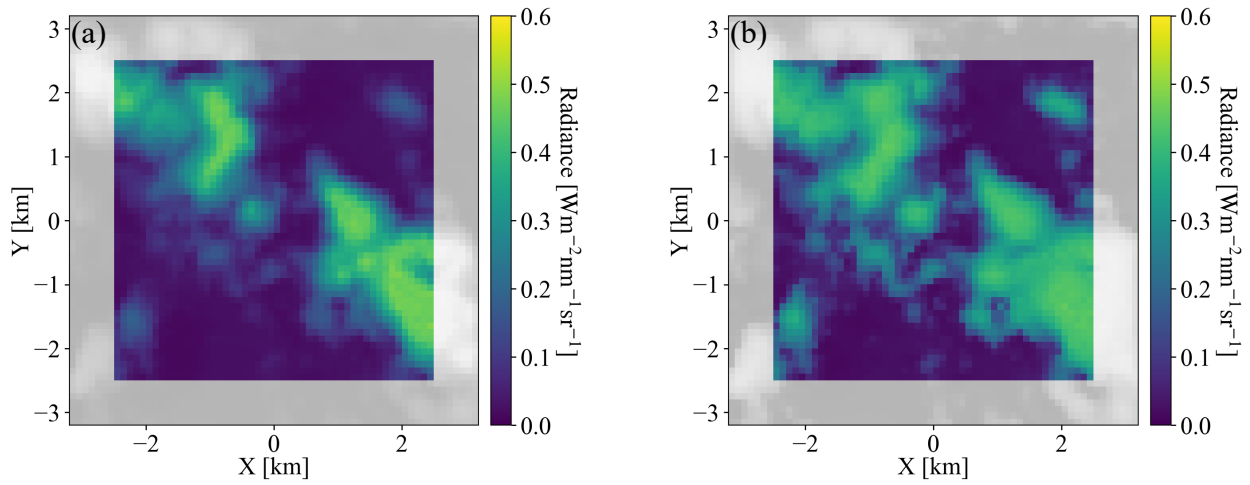
838

839

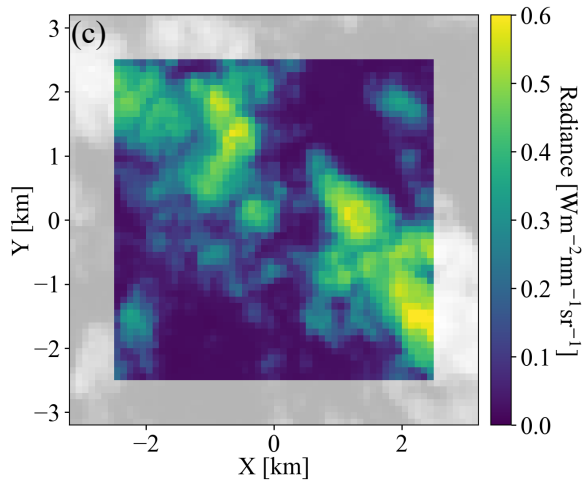
840

841

842



843

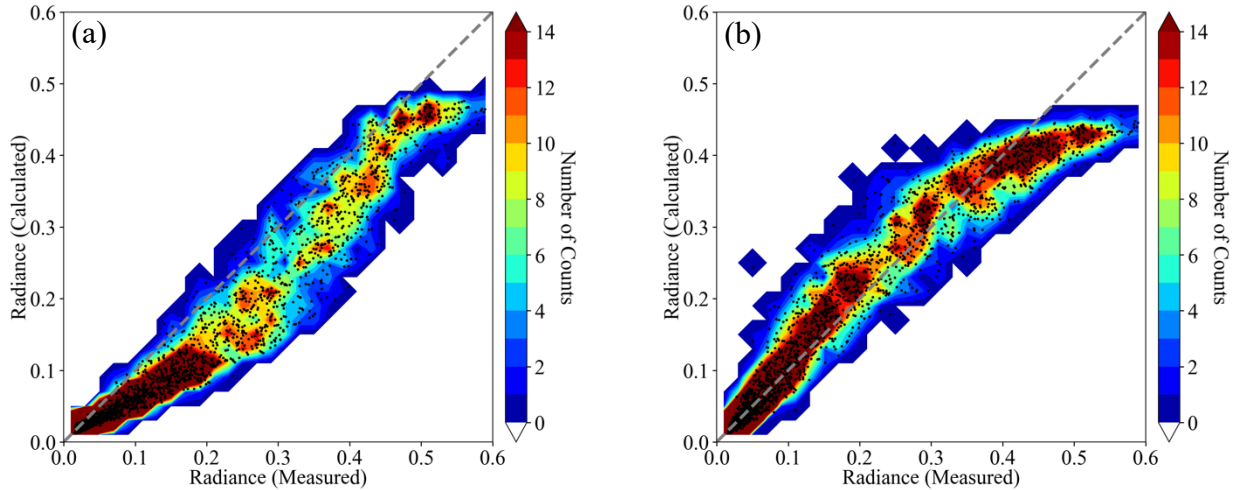


844

845 **Figure 12.** 3D radiance calculations from EaR³T at 600 nm based on cloud optical thickness field **(a)** estimated by
846 IPA, and **(b)** predicted by the CNN. The radiance measured by the all-sky camera (the same as Figure
847 10b) is provided in the same format at **(c)** for comparison. The calculations were originally performed
848 for the 64x64 domain. Then 7 pixels along each side of the domain (contoured in gray),
849 which resulted in a 50x50 domain.

850

851

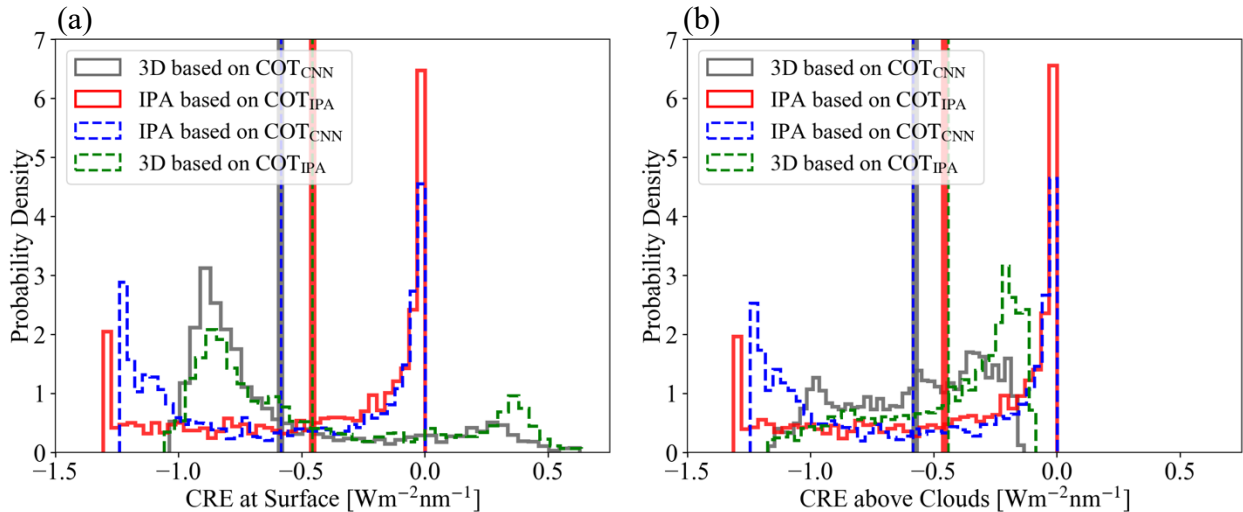


852
 853 **Figure 13.** Scatter plot overlays 2D histogram of 3D radiance calculations at 600 nm based on cloud optical thickness
 854 **(a)** estimated by IPA and **(b)** predicted by the CNN vs. measured red channel radiance from all-sky camera.
 855

856 As evident from the brightest pixels in Figures 12b and 12c, the radiances simulated on the
 857 basis of the CNN COT input are markedly lower than actually observed by the camera. This is
 858 because the CNN was trained on a LES dataset with limited COT range that excluded the largest
 859 COT that occurred in practice. This means that the observational data went beyond the original
 860 training envelope of the CNN, which highlights the importance of choosing the CNN training data
 861 carefully for a given region. In Figure 13, the simulations are directly compared with the original
 862 observations, confirming that indeed the CNN-generated data are below the observations on the
 863 high radiance end. Otherwise, the CNN-generated radiances agree with the observations. In
 864 contrast, the IPA-generated data are systematically lower than the observations, over the dynamic
 865 range of the COT, which is indicative of the 3D retrieval bias that we discussed earlier. Here again,
 866 the self-consistency approach proves useful despite the absence of ground truth data for the COT.
 867 This is extremely helpful because in reality satellite remote sensing does not have the ground truth
 868 of COT, whereas radiance measurements are always available. For the CNN, the self-consistency
 869 of the radiance is remarkable for the thinner clouds (radiance smaller than 0.4), which encompass
 870 83.5% of the total number of image pixels.

871 Finally, we use EaR³T to propagate the 3D cloud retrieval bias into the associated bias in
 872 estimating the cloud radiative effect from passive imagery retrievals, which means that we are
 873 returning from a remote sensing to an energy perspective (irradiance) at the end of the paper. The
 874 calculated cloud radiative effects (CRE) of both below-clouds (at the surface) and above-clouds

875 (at 3 km) are shown in Figure 14a and 14b. The most important histograms are those from 3D
 876 irradiance calculations based on the CNN retrievals (gray solid line), as this combination would
 877 be used in a next-generation framework for deriving CRE from passive remote sensing, and the
 878 other would be IPA irradiance calculations based on the IPA retrieval (red solid line), as done in
 879 the traditional (heritage) approach. The dashed lines are the other combinations. The mean values
 880 (red vs. gray) indicate that in our case the traditional approach would lead to a high bias of more
 881 than to 25% both at the surface and above clouds. Here again, 3D biases do not cancel each other
 882 out in the domain average. If the CNN had better fidelity even for optically thick clouds, the real
 883 bias in CRE would be even larger. A minor, but interesting finding is that regardless of which COT
 884 retrieval is used, the mean CRE is very similar for IPA and 3D irradiance calculations (e.g.,
 885 $\overline{CRE_{IPA}(COT_{CNN})} \approx \overline{CRE_{3D}(COT_{CNN})}$, blue dashed line overlay gray solid line), even though the
 886 PDFs are very dissimilar. By far the largest impact on accuracy comes from the retrieval technique,
 887 not from the subsequent CRE calculations. Here again, the self-consistency check turns out as a
 888 powerful metric to assess retrieval accuracy. Of course, we only used a single case in this part of
 889 the paper. For future evaluation of the CNN versus the IPA, one would need to process larger
 890 quantities of data in an automated fashion as done in the first part of the paper. This is beyond the
 891 scope of this introductory paper, and will be included in future releases of EaR³T and the CNN.
 892



893
 894 **Figure 14.** Histograms of cloud radiative effects derived from 1) 3D irradiance calculations based on COT_{CNN} (solid
 895 gray), 2) IPA irradiance calculations based on COT_{IPA} (solid red), 3) IPA irradiance calculations based on
 896 COT_{CNN} (dashed blue), and 4) 3D irradiance calculations based on COT_{IPA} (dashed green) both (a) at the
 897 surface and (b) above the clouds. The mean values are indicated by vertical lines.

898

899 7. Summary and Conclusion

900 In this paper, we introduced EaR³T, a toolbox that provides high-level interfaces to
901 automate and facilitate 1D- and 3D-RT calculations. We presented applications that used EaR³T
902 to:

- 903 a) build a processing pipeline that can automatically simulate 3D radiance fields for satellite
904 instruments (currently OCO-2 and MODIS) from publicly available satellite surface and
905 cloud products at any given time over any specific region;
- 906 b) build a processing pipeline that can automatically simulate irradiance along all flight legs
907 of aircraft missions, based on geostationary cloud products;
- 908 c) simulate radiance and irradiance for high-resolution COT fields retrieved from an airborne
909 camera, using both a traditional 1D-RT (IPA) approach, and a newly developed 3D-RT
910 (CNN) approach that considers the spatial context of a pixel.

911 Unlike other satellite simulators that employ 1D-RT, EaR³T is capable of performing the radiance
912 and irradiance calculations in 3D-RT mode. Optionally, it can be turned off to link back to
913 traditional 1D-RT codes, and to calculate 3D perturbations by considering the changes of 3D-RT
914 fields relative to the 1D-RT baseline.

915 With the processing pipeline under a) (App. 1 and App. 2, section 4), we prototyped a
916 3D-RT powered radiance loop that is envisioned for upcoming satellite missions such as
917 EarthCARE and AOS. Retrieved cloud fields (in our case, from MODIS and from an airborne
918 camera) are fed back into a 3D-RT simulation engine to calculate at-sensor radiances, which are
919 then compared with the original measurements. Beyond currently included sensors, others can be
920 added easily, taking advantage of the modular design of EaR³T. This radiance closure loop
921 facilitates the evaluation of passive imagery products, especially under spatially inhomogeneous
922 cloud conditions. The automation of EaR³T permits calculations at any time and over any given
923 region, and statistics can be built by looping over entire orbits as necessary. The concept of
924 radiance consistency could be valuable even for existing imagery datasets because it allows the
925 automated quantification of 3D-RT biases even without ground truth such as airborne irradiance
926 from suborbital activities. In the future it should be possible to include a 3D-RT pipeline such as
927 EaR³T into operational processing of satellite derived data products.

928 Benefitting from the automation of EaR³T in b) (App. 3, section 5), we performed 3D-RT
929 irradiance calculations for the entire CAMP²Ex field campaign, moving well beyond radiation

930 closure case studies, and instead systematically evaluating satellite-derived radiation fields with
931 aircraft data for an entire region. From the comparison based on all below-cloud flight tracks
932 during the entire campaign, we found that the satellite-derived cloud transmittance was biased low
933 by 10% compared to the observations when relying on the heritage satellite cloud product.

934 From the statistical results of the CAMP²Ex irradiance closure in b), we concluded that the
935 bias between satellite-derived irradiances and the ground truth from aircraft measurements was
936 due to a combination of the coarse spatial resolution of the geostationary imagery products and
937 3D-RT effects. To minimize the coarse-resolution part of the bias and thus to isolate the 3D-RT
938 bias, we used high-resolution airborne camera imagery in c) (App. 4, section 6), and found that
939 even with increased imager resolution, biases persisted. The at-sensor radiance derived from IPA
940 COT retrievals was inconsistent with the original measurements. For cloudy pixels, the calculated
941 radiance was well below the observations, confirming an overall low bias in IPA COT. This low
942 bias could be largely mitigated with the context-aware CNN developed separately in Nataraja et
943 al. (2022) and included in EaR³T. Of course, this novel technique has limitations. For example,
944 the camera reflectance data went beyond the CNN training envelope, which would need to be
945 extended to larger COT in the future. In addition, the CNN only reproduces two-dimensional
946 clouds fields and does not provide access to the vertical dimension, which will be the next frontier
947 to tackle. Still, the greatly improved radiance consistency from COT_{IPA} to COT_{CNN} indicates that
948 the EaR³T-LES-CNN approach shows great promise for the mitigation of 3D-RT biases associated
949 with heritage cloud retrievals. We also discovered that for this particular case, the CRE calculated
950 from traditional 1D cloud products can introduce a warm bias of at least 25% at the surface and
951 above clouds.

952 EaR³T has proven to be capable of facilitating 3D-RT calculations for both remote sensing
953 and radiative energy studies. Beyond the applications described in this paper, EaR³T has already
954 been extensively used by a series of on-going research projects such as producing massive 3D-RT
955 calculations as training data for a new generation of CNN models (Nataraja et al., 2022), evaluating
956 3D cloud radiative effects associated with aerosols (Gristey et al., 2022), creating flight track and
957 satellite track simulations for mission planning etc. More importantly, the strategies provided in
958 this paper put novel machine learning algorithms on a physical footing, opening the door for the
959 mitigation of complexity-induced biases in the near-future. More development effort will be
960 invested into EaR³T in the future, with the goals of minimizing the barriers to using 3D-RT

961 calculations, and to promote 3D cloud studies. EaR³T will continue to be an educational tool driven
962 by graduate students. In the future, we plan to add support for additional publicly available 3D RT
963 solvers, e.g., SHDOM, as well as built-in support for HITRAN and associated correlated-k
964 methods. From a research perspective, we anticipate that EaR³T will enable the systematic
965 quantification and mitigation of 3D-RT biases of imagery-derived cloud-aerosol radiative effects,
966 and may be the starting point for operational use of 3D-RT for future satellite missions.
967

968 **Appendix A - Technical Input Parameters of EaR³T**

969 EaR³T provides various functions that can be combined to tailored pipelines for automatic
970 3D radiative transfer (3D-RT) calculations as described App. 1 – 5 of this paper (App. 1 – 5), as
971 well as for complex research projects beyond. Since EaR³T is written in Python, the modules and
972 functions can be integrated into existing functions developed by the users themselves.
973 Parallelization is enabled in EaR³T by default through multi-processing to accelerate computations.
974 If multiple CPUs are available, EaR³T will distribute jobs for the 3D RT calculations. By default,
975 the maximum number of CPUs will be used. Since EaR³T is designed to make the process of
976 setting up and running 3D-RT calculations simple, some parameters that are unavailable from the
977 input data but are required by the RT solvers are populated via default values and assumptions.
978 However, this does not mean that by using EaR³T, one must use these assumptions; they can be
979 easily superseded by user-provided settings. To facilitate this process, Table A1 provides a detailed
980 list of parameters (subject to change in future updates) that can be controlled and modified by the
981 user. In `examples/02_modis_rad-sim.py`, we defined these user-controllable parameters
982 as global variables for providing easy access to user. In the future, most of the parameters will be
983 controllable through a dedicated configuration file for optimal transparency. These parameters can
984 be changed within the code. For instance, by changing the parameters of `_date` (Line 67 in
985 `examples/02_modis_rad-sim.py`) and `_region` (Line 68 in
986 `examples/02_modis_rad-sim.py`) into the following:

```
987 _date = datetime.datetime(2022, 2, 10)  
988 _region = [-6.8, -2.8, 17.0, 21.0]
```

989 one can perform similar RT calculations (as demonstrated in App. 2) for another date and region
990 of interest (here, west Sahara Desert on 10 February, 2022). Note that the cloud detection
991 algorithms we included in the code are imperfect (they only work satisfactorily for the App. 2 case
992 we presented in this paper); for other regions on the globe, they may need to be adjusted.
993 Automation of this feature is planned for the future. In addition, intuitive and simple examples are
994 provided in `examples/00_er3t_mca.py` and `examples/00_er3t_lrt.py` for users
995 who are interested in learning the basics of setting up EaR³T for calculations. At the current stage,
996 only limited documentation is provided. However, community support is available from the author
997 of this paper through Discord⁶. In the near-future, more effort will be invested into documentation

⁶ <https://discord.gg/ntqsguwaWv>

998 to give the user more autonomy in creating new applications that cannot be derived from those
 999 provided in our paper.
 1000

Parameters	App. 1	App. 2	App. 3	App. 4	App. 5
	examples/01_oc o2_rad-sim.py	examples/02_mo dis_rad-sim.py	examples/03_sp ns_flux-sim.py	examples/04_ca m_nadir_rad- sim.py	examples/05_cn n-les_rad- sim.py
Date	September 2, 2019 Specified at Line 667: date And Line 626: date	September 2, 2019 Specified at Line 67: _date And Line 500: date	September 20, 2019 Specified at Line 442: date And Line 241: date	October 5, 2019 Specified at Line 390: date And Line 233: date	August 29, 2016 Specified at Line 222: date
Geographical Region	Specified at Line 668: extent	Specified at Line 68: _region	Variable (depends on aircraft location)	N/A	N/A
Z Grid (Number of Grids/Resolut ion)	40 / 0.5 km Specified at Line 547: levels	40 / 0.5 km Specified at Line 422: levels	20 / 1 km Specified at Line 184: levels	40 / 0.5 km Specified at Line 192: levels	20 / 1km Specified at Line 197: levels
Wavelength	770 nm Specified at Line 785: wavelength	650 nm Specified at Line 70: wavelength	745 nm Specified at Line 443: wavelength	600 nm Specified at Line 57: wavelength	600 nm Specified at Line 62: wv10
Atmospheric Gas Profile	US standard atmosphere Specified at Line 549: atm0	US standard atmosphere Specified at Line 424: atm0	US standard atmosphere Specified at Line 186: atm0	US standard atmosphere Specified at Line 194: atm0	US standard atmosphere Specified at Line 200: atm0
Atmospheric Gas Absorption	Case specific Specified at Line 557: abs0	Default Absorption Database (Coddington et al., 2008) Specified at Line 431: abs0	Default Absorption Database (Coddington et al., 2008) Specified at Line 192: abs0	Default Absorption Database (Coddington et al., 2008) Specified at Line 201: abs0	Default Absorption Database (Coddington et al., 2008) Specified at Line 200: abs0
Cloud Top Height	From MODIS L2 cloud product Specified at Line 306: cth_2d_12 And Line 592: cld0	From MODIS L2 cloud product Specified at Line 280: cth_2d_12 And Line 466: cld0	From AHI L2 cloud product Specified at Line 211: cth_2d And Lines 215: cld0	2 km Specified at Line 217: cth And Lines 217: cld0	From LES Specified at Line 205: cld0
Cloud Geometrical Thickness	1 km Specified at Line 592: cgt	1 km And Line 466: cgt	1 km Specified at Line 215: cgt	1 km Specified at Line 217: cgt	From LES Specified at Line 205: cld0
Cloud Optical Thickness	Two-Stream Approximation for MODIS L1B Reflectance at 250 m resolution Specified at Line 402: cot_2d_11b And Line 592: cld0	Two-Stream Approximation for MODIS L1B Reflectance at 250 m resolution Specified at Line 337: cot_2d_11b And Line 466: cld0	From AHI L2 cloud product Specified at Line 201: cot_2d And Lines 215: cld0	Two-Stream Approximation and CNN for camera red channel radiance/reflectance at 100 m resolution Specified at Lines 285 and 324: cot_ipa and cot_wei And Lines 217: cld0	From LES Specified at Line 205: cld0
Cloud Effective Radius	From MODIS L2 Cloud Product Specified at Line 313: cer_2d_12	From MODIS L2 Cloud Product Specified at Line 287: cer_2d_12	From AHI L2 cloud product Specified at Line 202: cer_2d	12 micron Specified at Lines 285 and 380:	From LES Specified at Line 205: cld0

	And Line 592: cld0	And Line 466: cld0	And Lines 215: cld0	cer_ipa and cer_2d And Lines 217: cld0	
Scattering Phase Function	Mie Specified at Line 598: pha0 And Line 630: sca	Mie Specified at Line 472: pha0 And Line 504: sca	Mie Specified at Line 222: pha0 And Line 240: sca	Henyey-Greenstein (g=0.85) Implicitly specified by default at Line 232: mcarats_ng Notes: Lines 207, 208, and 237 can be uncommented (meanwhile commenting out Line 209) to turn on Mie	Henyey-Greenstein (g=0.85) Implicitly specified by default at Line 221: mcarats_ng
Surface Albedo	From MODIS Surface Reflectance product and scaled by OCO-2 Specified at Line 520: oco_sfc_alb_2d And Line 629: sfc_2d	From MODIS Surface Reflectance product Specified at Line 395: mod_sfc_alb_2d And Line 503: sfc_2d	0.03 Implicitly specified by default at Line 237: mcarats_ng	0.03 Specified at Line 236: surface_albedo	0 Specified at Line 227: surface_albedo
Solar Zenith Angle	From OCO-2 geolocation file Specified at Line 615: sza And Line 633: solar_zenith_a ngle	From MODIS geolocation file Specified at Line 489: sza And Line 507: solar_zenith_a ngle	Variable (depends on aircraft location and date and time)	28.90° Specified at Line 352: geometry['sza'] And Line 240: solar_zenith_a ngle	29.16° Specified at Line 228: solar_zenith_a ngle
Solar Azimuth Angle	From OCO-2 geolocation file Specified at Line 616: saa And Line 634: solar_azimuth_ angle	From MODIS geolocation file Specified at Line 490: saa And Line 508: solar_azimuth_ angle	Variable (depends on aircraft location and date and time)	296.83° Specified at Line 353: geometry['saa'] And Line 241: solar_azimuth_ angle	296.83° Specified at Line 229: solar_azimuth_ angle
Sensor Altitude	705 km (satellite altitude) Implicitly specified by default at Line 625: mcarats_ng	705 km (satellite altitude) Implicitly specified by default at Line 499: mcarats_ng	N/A, three- dimensional irradiance outputs at user-defined Z grid	5.48 km (flight altitude) Specified at Line 354: geometry['alt'] And Line 242: sensor_altitud e	705 km (satellite altitude) Implicitly specified by default at Line 221: mcarats_ng
Sensor Zenith Angle	From OCO-2 geolocation file Specified at Line 617: vza And Line 635: sensor_zenith_ angle	From MODIS geolocation file Specified at Line 491: vza And Line 509: sensor_zenith_ angle	0° (nadir) Implicitly specified by default at Line 237: mcarats_ng	0° (nadir) Implicitly specified by default at Line 232: mcarats_ng	0° (nadir) Specified at Line 230: sensor_zenith_ angle
Sensor Azimuth Angle	From OCO-2 geolocation file Specified at Line 618: vaa	From MODIS geolocation file Specified at Line 492: vaa	0° (insignificant for nadir)	0° (insignificant for nadir)	0° (insignificant for nadir) Specified at Line 231:

	And Line 636: sensor_azimuth_angle	And Line 510: sensor_azimuth_angle	Implicitly specified by default at Line 237: mcarats_ng	Implicitly specified by default at Line 232: mcarats_ng	sensor_azimuth_angle
Number of Photons	1×10^8 per run Specified at Line 72: photon_sim And Line 640: photons	1×10^8 per run Specified at Line 71: _photon_sim And Line 514: photons	1×10^7 per run Specified at Line 56: photon_sim And Line 246: photons	1×10^8 per run Specified at Line 56: _photon_sim And Line 246: photons	1×10^8 per run Specified at Line 66: photon_sim And Line 234: photons
Number of Runs	3 Specified at Line 638: Nrun	3 Specified at Line 512: Nrun	3 Specified at Line 245: Nrun	3 Specified at Line 244: Nrun	3 Specified at Line 233: Nrun
Mode (3D or IPA)	3D and IPA Specified at Line 786: solver And Line 641: solver	3D Specified at Line 620: solver And Line 515: solver	3D and IPA Specified at Lines 380 and 381: solver And Line 247: solver	3D Specified at Lines 391 and 392: solver And Line 247: solver	3D Specified at Line 210: solver And Line 236: solver
Parallelization Mode	Python multi-processing Specified at Line 643: mp_mode	Python multi-processing Specified at Line 517: mp_mode	Python multi-processing Specified at Line 250: mp_mode	Python multi-processing Specified at Line 249: mp_mode	Python multi-processing Specified at Line 238: mp_mode
Number of CPUs	8 Specified at Line 642: Ncpu	8 Specified at Line 516: Ncpu	16 Specified at Line 314: Ncpu And Line 249: Ncpu	12 Specified at Line 248: Ncpu	24 on clusters Specified at Line 237: Ncpu

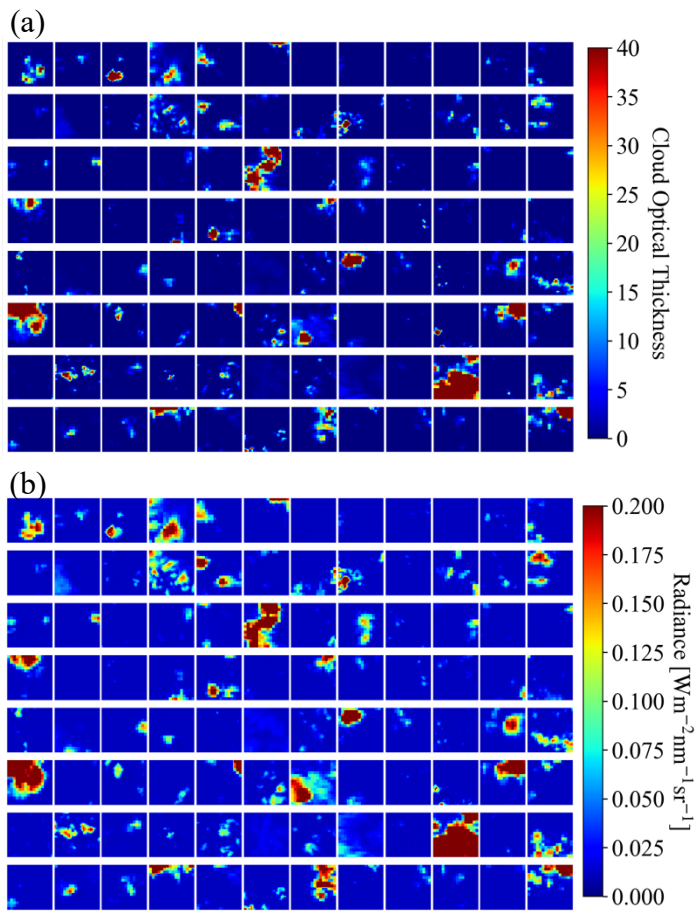
1001
1002 **Table A1:** List of parameters used in the five applications. The line numbers used in the table are referring to the code
1003 script of each application. If two line numbers are provided, the first one indicates where the parameter is
1004 defined and the second one indicates where the parameter is passed into the radiative transfer setup. Users
1005 can change either one for customization purposes.

1006
1007 **Appendix B – App. 5 Radiance calculations based on the Large Eddy Simulation**

1008 The CNN COT retrieval framework was developed by Nataraja et al. (2022). It adapts a
1009 U-Net (Ronneberger et al., 2015) architecture and treats the retrieval of COT from radiance as a
1010 segmentation problem – probabilities of 36 COT classes (ranging from COT of 0 to 100) are
1011 returned as the final COT retrieved for a given cloud radiance field. It accounts for horizontal
1012 photon transport, which is neglected in traditional cloud retrieval algorithms; in other words, for
1013 the spatial context of cloudy pixels. It was trained on synthetic cloud fields generated by a Large
1014 Eddy Simulation (LES) model, which provides the ground truth of COT. Subsequently, EaR³T was
1015 used to calculate 3D-RT radiances at 600 nm for LES cloud fields to establish a mapping between

1016 radiance to COT. Only six LES cases were used to represent the variability of the cloud
1017 morphology. Each of these fields are 480x480 pixels across (spatial resolution of 100 m). These
1018 large fields were mapped onto thousands of 64x64 mini tiles with spatial resolution of 100 m as
1019 described in Nataraja et al., 2022. To keep the training data set small, mini tiles selectively sampled
1020 according to their mean COT and standard deviation. This ensured an even representation of the
1021 dynamic range of COT and its variability, which was termed homogenization of the training data
1022 set. Figure A1 shows a collection of samples from the training data as an illustration. All the
1023 aforementioned simulation setup and techniques in data process are included in the App. 5 example
1024 code, which can be applied to the LES data (a different scene from the 6 scenes) distributed along
1025 with EaR³T.

1026



1027

1028

1029 **Figure A1.** Illustrations of 64x64 tiles of **(a)** cloud optical thickness from LES data and **(b)** calculated 3D radiance
1030 from EaR³T for CNN training.

1031

1032 **Appendix C**

1033 **C1. Cloud Detection/Identification**

1034 Cloudy pixels are identified through a simple thresholding method based on the red, green,
1035 and blue channels of MODIS. When the radiance values of the red, green, and blue channels of a
1036 pixel are all greater than the corresponding median value, the pixel is considered as cloudy, as
1037 illustrated by the following equation

$$1038 \quad \begin{array}{l} \text{If } Red > Median(Red) \ \& \\ \text{Blue} > Median(Blue) \ \& \\ \text{Green} > Median(Green) \end{array} \left\{ \begin{array}{l} \text{Yes, cloudy} \\ \text{No, clear sky} \end{array} \right. \quad (A1)$$

1039 Note that this only works for partially cloud-covered scenes, and may lead to false positives if
1040 there is brightness contrast from objects other than clouds. This method was specifically applied
1041 for the cases in this paper and should be changed as appropriate for future applications.

1042

1043 **C2. Two-Stream Approximation**

1044 The two-stream approximation of the reflectance R is calculated using Eq. D2 from Chen
1045 et al. (2021), as follows:

$$1046 \quad R = \frac{\tau + \alpha \cdot \left(\frac{2\mu}{(1-g) \cdot (1-\alpha)} \right)}{\tau + \left(\frac{2\mu}{(1-g) \cdot (1-\alpha)} \right)} \quad (A2)$$

1047 where τ is the cloud optical thickness, α is the surface albedo, μ is the cosine of the solar zenith
1048 angle, and g is the asymmetry parameter. A value of 0.85 is assumed for g . The domain average
1049 of the solar zenith angle and surface albedo are calculated and used for estimating μ and α . Then,
1050 for a range of τ , we calculated the R and obtained the relationship of $R(\tau)$. For those cloudy pixels
1051 identified through A1, the inverse relationship of $\tau(R)$ is then used for estimating τ at any given
1052 R . Note that this approach does not take into account any cloud reflectance anisotropies.

1053

1054 **Appendix D**

1055 **D1. Parallax Correction**

1056 From the satellite's view, the clouds (especially high clouds) will be placed at inaccurate
 1057 locations on the surface, which have shifted from their actual locations due to the parallax effect.
 1058 We followed simply trigonometry to correct for it, as follows:

1059 Longitude correction (positive from west to east):

$$1060 \quad \delta lon = \frac{(z_{cld} - z_{sfc}) \cdot \tan(\theta) \cdot \sin(\phi)}{\pi \cdot R_{Earth}} \times 180^\circ \quad (B1)$$

1061 Latitude correction (positive from south to north):

$$1062 \quad \delta lat = \frac{(z_{cld} - z_{sfc}) \cdot \tan(\theta) \cdot \cos(\phi)}{\pi \cdot R_{Earth}} \times 180^\circ \quad (B2)$$

1063 where $(lon_{sat}, lat_{sat}, z_{sat})$ is the satellite location and θ and ϕ (0° at north, positive clockwise)
 1064 are the sensor viewing zenith and azimuth angles. z_{cld} and z_{sfc} are the cloud top height and the
 1065 surface height. R_{Earth} is the radius of the Earth. Figure A2 shows an illustration of parallax
 1066 correction for the cloud field in the inset in Figure 2.

1067

1068 **D2. Wind Correction**

1069 The wind correction aims at correcting the movement of clouds when advected by the wind
 1070 between two different satellites' overpasses.

1071 Longitude correction (positive from west to east):

$$1072 \quad \delta lon = \frac{\bar{u} \cdot \delta t}{\pi \cdot R_{Earth}} \times 180^\circ \quad (B3)$$

1073 Latitude correction (positive from south to north):

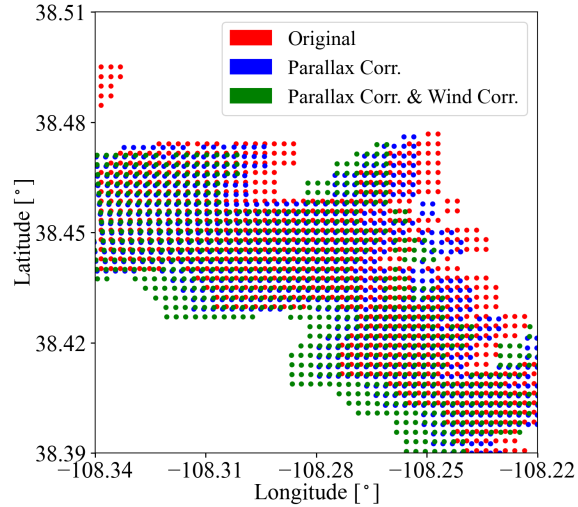
$$1074 \quad \delta lat = \frac{\bar{v} \cdot \delta t}{\pi \cdot R_{Earth}} \times 180^\circ \quad (B4)$$

1075 where \bar{u} and \bar{v} are the domain-averaged 10 m zonal and meridional wind speeds, and δt is the time
 1076 difference between two different satellites that fly on the same orbit. Figure A2 shows the cloud
 1077 location after applying the parallax (Appendix D1) and wind correction for the cloud field in the
 1078 inset from Figure 2.

1079

1080

1081



1082
 1083 **Figure A2.** An illustration of correcting cloud location (red) for parallax effect (blue) and wind effect (green) for the
 1084 cloud field of the inset in Figure 2.
 1085

1086
 1087

1088 **Acknowledgement**

1089 The aircraft all-sky camera was radiometrically calibrated by the U.S. Naval Research Laboratory.
 1090 We thank Jens Redemann for insightful discussions about Figure 9 (App. 3) about the apparent
 1091 contradiction of the direction of the COT, reflectance, and transmittance biases.
 1092

1093

1093 **Data availability**

1094 For App. 1 and App. 2, the OCO-2 data were provided by the NASA Goddard Earth Sciences Data
 1095 and Information Services Center (GES DISC, <https://oco2.gesdisc.eosdis.nasa.gov/data>) and the
 1096 MODIS data were provided by the NASA Goddard Space Flight Center's Level-1 and Atmosphere
 1097 Archive and Distribution System (LAADS, <https://ladsweb.modaps.eosdis.nasa.gov/archive>),
 1098 which are all publicly available and can be downloaded by EaR³T through the application code.
 1099 For App. 3, the AHI data were processed by Holz's (coauthor of this paper) team. The SPN-S data
 1100 were provided by Schmidt and Norgren (coauthors of this paper). Both the AHI and SPN-S data
 1101 are publicly available at NASA Airborne Science Data for Atmospheric Composition
 1102 (<https://www-air.larc.nasa.gov/missions/camp2ex/index.html>). The AHI data and the SPN-S data
 1103 for the flight track indicated in Figure 8 of the paper are distributed along with EaR³T for
 1104 demonstration purpose. For App. 4, all sky camera imagery and CNN model are distributed along

1105 with EaR³T. EaR³T is publicly available and can be accessed and downloaded at
1106 <https://github.com/hong-chen/er3t> (or <https://doi.org/10.5281/zenodo.7374196> for v0.1.0 used in
1107 this paper; Chen and Schmidt, 2022).

1108

1109 **Author contributions**

1110 All the authors helped with editing the paper. HC developed the EaR³T package in Python
1111 including the application code, performed the analysis, and wrote the majority of the paper with
1112 input from the other authors. SS provided MCARaTS simulation wrapper code in Interactive Data
1113 Language (IDL); helped with the structure design of EaR³T; and helped with interpreting the
1114 results and writing the paper. SM helped with the OCO-2 data interpretation. VN trained and
1115 provided the CNN model. MN helped with the SPN-S instrument calibration and data processing.
1116 JG and GF helped with testing EaR³T and the LES data interpretation. RH provided the AHI data
1117 and helped with the data interpretation. HI helped with the implementation of MCARaTS into
1118 EaR³T.

1119 **References**

- 1120 Anderson, G. P., Clough, S. A., Kneizys, F. X., Chetwynd, J. H., and Shettle, E. P.: AFGL
1121 atmospheric constituent profiles (0–120 km), Tech. Rep. AFGL-TR-86–0110, Air Force
1122 Geophys. Lab., Hanscom Air Force Base, Bedford, Massachusetts, U.S.A., 1986.
- 1123 Barker, H. and Liu, D.: Inferring optical depth of broken clouds from Landsat data, *J. Climate*, 8,
1124 2620–2630, 1995.
- 1125 Barker, H. W., Jerg, M. P., Wehr, T., Kato, S., Donovan, D. P., and Hogan, R. J.: A 3D cloud
1126 construction algorithm for the EarthCARE satellite mission, *Q. J. Roy. Meteor. Soc.*, 137,
1127 1042– 1058, <https://doi.org/10.1002/qj.824>, 2011.
- 1128 Barker, H. W., Kato, S., and Wehr, T.: Computation of solar radiative fluxes by 1-D and 3-D
1129 methods using cloudy atmospheres inferred from A-train satellite data, *Surv. Geophys.*, 33,
1130 657–676, 2012.
- 1131 Cahalan, R., Oreopoulos, L., Marshak, A., Evans, F., Davis, A., Pincus, R., Yetzen, K. H., Mayer,
1132 B., Yetzer, K. H., Mayer, B., Davies, R., Ackerman, T. P., Barker, H. W., Clothiaux, E. E.,
1133 Ellingson, R. G., Garay, M. J., Kassianov, E., Kinne, S., Macke, A., O'Hirok, W., Partain, P.
1134 T., Prigarin, S. M., Rublev, A. N., Stephens, G. L., Szczap, F., Takara, E. E., Varnai, T., Wen,
1135 G., and Zhuravleva, T.: The I3RC: Bringing Together the Most Advanced Radiative Transfer
1136 Tools for Cloudy Atmospheres, *B. Am. Meteorol. Soc.*, 86, 1275–1293, 2005.
- 1137 Chen, H. and Schmidt, S.: er3t-v0.1.0, <https://doi.org/10.5281/zenodo.7374196>, 2022.
- 1138 Chen, H., Schmidt, S., and Holz, R. E.: Synchronized Flight Videos for NASA CAMP²Ex,
1139 <https://doi.org/10.5281/zenodo.7358509>, 2022.
- 1140 Crisp, D.: Measuring Atmospheric Carbon Dioxide from Space with the Orbiting Carbon
1141 Observatory-2 (OCO-2), *P. Soc. Photo.-Opt. Ins.*, 9607, 960702,
1142 <https://doi.org/10.1117/12.2187291>, 2015.
- 1143 Coddington, O., Schmidt, K. S., Pilewskie, P., Gore, W. J., Bergstrom, R., Roman, M., Redemann,
1144 J., Russell, P. B., Liu, J., and Schaaf, C. C.: Aircraft measurements of spectral surface albedo
1145 and its consistency with ground-based and space-borne observations, *J. Geophys. Res.*, 113,
1146 D17209, doi:10.1029/2008JD010089, 2008.
- 1147 Deneke, H., Barrientos-Velasco, C., Bley, S., Hünerbein, A., Lenk, S., Macke, A., Meirink, J. F.,
1148 Schroedter-Homscheidt, M., Senf, F., Wang, P., Werner, F., and Witthuhn, J.: Increasing the
1149 spatial resolution of cloud property retrievals from Meteosat SEVIRI by use of its high-

1150 resolution visible channel: implementation and examples, *Atmos. Meas. Tech.*, 14, 5107–
1151 5126, <https://doi.org/10.5194/amt-14-5107-2021>, 2021.

1152 Deutschmann, T., Beirle, S., Friess, U., Grzegorski, M., Kern, C., Kritten, L., Platt, U., Prados-
1153 Roman, C., Pukite, J., Wagner, T., Werner, B., and Pfeilsticker, K.: The Monte Carlo
1154 atmospheric radiative transfer model McArtim: introduction and validation of Jacobians and
1155 3-D features, *J. Quant. Spectrosc. Ra.*, 112(6), 1119–1137, ISSN 0022-4073,
1156 doi:10.1016/j.jqsrt.2010.12.009, 2011.

1157 Doicu, A., Efremenko, D., and Trautmann, T.: A multi-dimensional vector spherical harmonics
1158 discrete ordinate method for atmospheric radiative transfer, *J. Quant. Spectrosc. Ra.*, 118,
1159 121–131, <https://doi.org/10.1016/j.jqsrt.2012.12.009>, 2013.

1160 Emde, C., Barlakas, V., Cornet, C., Evans, F., Korokin, S., Ota, Y., Labonnote, L. C., Lyapustin,
1161 A., Macke, A., Mayer, B., and Wendisch, M.: IPRT polarized radiative transfer model
1162 intercomparison project – Phase A, *Journal of Quantitative Spectroscopy and Radiative*
1163 *Transfer*, 164, 8–36, <https://doi.org/10.1016/j.jqsrt.2015.05.007>, 2015.

1164 Emde, C., Buras-Schnell, R., Kylling, A., Mayer, B., Gasteiger, J., Hamann, U., Kylling, J., Richter,
1165 B., Pause, C., Dowling, T., and Bugliaro, L.: The libRadtran software package for radiative
1166 transfer calculations (version 2.0.1), *Geosci. Model Dev.*, 9, 1647–1672,
1167 <https://doi.org/10.5194/gmd-9-1647-2016>, 2016.

1168 Evans, K. F.: The spherical harmonics discrete ordinate method for three-dimensional atmospheric
1169 radiative transfer, *J. Atmos. Sci.*, 55, 429–446, 1998.

1170 Gatebe, C. K., Jethva, H., Gautam, R., Poudyal, R., and Várnai, T.: A new measurement approach
1171 for validating satellite-based above-cloud aerosol optical depth, *Atmos. Meas. Tech.*, 14,
1172 1405–1423, <https://doi.org/10.5194/amt-14-1405-2021>, 2021.

1173 Gristey, J. J., Feingold, G., Glenn, I. B., Schmidt, K. S., and Chen, H.: Surface Solar Irradiance in
1174 Continental Shallow Cumulus Fields: Observations and Large-Eddy Simulation, *J. Atmos.*
1175 *Sci.*, 77, 1065–1080, <https://doi.org/10.1175/JAS-D-19-0261.1>, 2020a.

1176 Gristey, J. J., Feingold, G., Glenn, I. B., Schmidt, K. S., and Chen, H.: On the Relationship
1177 Between Shallow Cumulus Cloud Field Properties and Surface Solar Irradiance, *Geophysical*
1178 *Research Letters*, 47, e2020GL090152, <https://doi.org/10.1029/2020GL090152>, 2020b.

1179 Gristey, J. J., Feingold, G., Glenn, I. B., Schmidt, K. S., and Chen, H.:
1180 Influence of Aerosol Embedded in Shallow Cumulus Cloud Fields on the Surface Solar

1181 Irradiance, *Journal of Geophysical Research: Atmospheres*, 127, e2022JD036822,
1182 <https://doi.org/10.1029/2022JD036822>, 2022.

1183 Heidinger, A. K., Foster, M. J., Walther, A., and Zhao, X.: The Pathfinder Atmospheres-Extended
1184 AVHRR climate dataset, *B. Am. Meteorol. Soc.*, 95, 909–922,
1185 <https://doi.org/10.1175/BAMS-D-12-00246.1>, 2014.

1186 Illingworth, A. J., Barker, H. W., Beljaars, A., Chepfer, H., Delanoe, J., Domenech, C., Donovan,
1187 D. P., Fukuda, S., Hidakata, M., Hogan, R. J., Huenerbein, A., Kollias, P., Kubota, T.,
1188 Nakajima, T., Nakajima, T. Y., Nishizawa, T., Ohno, Y., Okamoto, H., Oki, R., Sato, K.,
1189 Satoh, M., Wandinger, U., Wehr, T., and van Zadelhoff, G.: The EarthCARE Satellite: the
1190 next step forward in global measurements of clouds, aerosols, precipitation and radiation, *B.*
1191 *Am. Meteorol. Soc.*, 96, 1311–1332, <https://doi.org/10.1175/BAMS-D-12-00227.1>, 2015.

1192 Iwabuchi, H.: Efficient Monte Carlo methods for radiative transfer modeling, *J. Atmos. Sci.*, 63,
1193 2324–2339, 2006.

1194 Kindel, B. C., Schmidt, K. S., Pilewskie, P., Baum, B. A., Yang, P., and Platnick, S.: Observations
1195 and modeling of ice cloud shortwave spectral albedo during the Tropical Composition, Cloud
1196 and Climate Coupling Experiment (TC⁴), *J. Geophys. Res.*, 115, D00J18,
1197 [doi:10.1029/2009JD013127](https://doi.org/10.1029/2009JD013127), 2010.

1198 King, M., and Platnick, S.: The Earth Observing System (EOS), *Comprehensive Remote Sensing*,
1199 7, 26, [doi:10.1016/b978-0-12-409548-9.10312-4](https://doi.org/10.1016/b978-0-12-409548-9.10312-4), 2018.

1200 Levis, A., Schechner, Y. Y., Davis, A. B., and Loveridge, J.: Multi-View Polarimetric Scattering
1201 Cloud Tomography and Retrieval of Droplet Size, *Remote Sens.*, 12, 2831,
1202 <https://doi.org/10.3390/rs12172831>, 2020.

1203 Li, J., Scinocca, J., Lazare, M., McFarlane, N., von Salzen, K., and Solheim, L.: Ocean Surface
1204 Albedo and Its Impact on Radiation Balance in Climate Models, *J. Climate*, 19, 6314–6333,
1205 2006.

1206 Long, C. N., Bucholtz, A., Jonsson, H., Schmid, B., Vogelmann, A., and Wood, J.: A Method of
1207 Correcting for Tilt from Horizontal in Downwelling Shortwave Irradiance Measurements on
1208 Moving Platforms, *The Open Atmospheric Science Journal*, 4, 78–87, 2010.

1209 Loveridge, J., Levis, A., Di Girolamo, L., Holodovsky, V., Forster, L., Davis, A. B., and Schechner,
1210 Y. Y.: Retrieving 3D distributions of atmospheric particles using Atmospheric Tomography
1211 with 3D Radiative Transfer – Part 1: Model description and Jacobian calculation, *Atmos.*

1212 Meas. Tech. Discuss. [preprint], <https://doi.org/10.5194/amt-2022-251>, in review, 2022.

1213 Masuda, R., Iwabuchi, H., Schmidt, K. S., Damiani, A. and Kudo, R.: Retrieval of Cloud Optical
1214 Thickness from Sky-View Camera Images using a Deep Convolutional Neural Network
1215 based on Three-Dimensional Radiative Transfer, *Remote Sensing*, 11(17), 1962,
1216 doi:10.3390/rs11171962, 2019.

1217 Marshak, A., Davis, A., Wiscombe, W., and Cahalan, R.: Radiative smoothing in fractal clouds, *J.*
1218 *Geophys. Res.*, 100, 26247–26261, <https://doi.org/10.1029/95JD02895>, 1995.

1219 Marshak, A., Wen, G., Coakley, J., Remer, L., Loeb, N. G., and Cahalan, R. F.: A simple model
1220 for the cloud adjacency effect and the apparent bluing of aerosols near clouds, *J. Geophys.*
1221 *Res.*, 113, D14S17, <https://doi.org/10.1029/2007JD009196>, 2008.

1222 Massie, S. T., Schmidt, K. S., Eldering, A., and Crisp, D.: Observational evidence of 3-D cloud
1223 effects in OCO-2 CO₂ retrievals, *J. Geophys. Res. Atmos.*, 122, 7064–7085,
1224 <https://doi.org/10.1002/2016JD026111>, 2017.

1225 Mayer, B. and Kylling, A.: Technical note: The libRadtran software package for radiative transfer
1226 calculations – description and examples of use, *Atmos. Chem. Phys.*, 5, 1855–1877,
1227 <https://doi.org/10.5194/acp-5-1855-2005>, 2005.

1228 Mayer, B.: Radiative transfer in the cloudy atmosphere, *EPJ Web of Conferences*, 1, 75–99,
1229 doi:10.1140/epjconf/e2009-00912-1, 2009.

1230 Mlawer, E. J., Taubman, S. J., Brown, P. D., Iacono, M. J., and Clough, S. A.: Radiative transfer
1231 for inhomogeneous atmospheres: RRTM, a validated correlated-k model for the longwave, *J.*
1232 *Geophys. Res.*, 102, 16663–16682, 1997.

1233 Nakajima, T. and King, M. D.: Determination of the optical thickness and effective particle radius
1234 of clouds from reflected solar radiation measurements. Part I: Theory, *J. Atmos. Sci.*, 47,
1235 1878–1893, 1990.

1236 Nataraja, V., Schmidt, S., Chen, H., Yamaguchi, T., Kazil, J., Feingold, G., Wolf, K., and Iwabuchi,
1237 H.: Segmentation-Based Multi-Pixel Cloud Optical Thickness Retrieval Using a
1238 Convolutional Neural Network, *Atmos. Meas. Tech.*, 15, 5181–5205, doi:10.5194/amt-15-
1239 5181-2022, 2022.

1240 Norgren, M. S., Wood, J., Schmidt, K. S., van Diedenhoven, B., Stamnes, S. A., Ziemba, L. D.,
1241 Crosbie, E. C., Shook, M. A., Kittelman, A. S., LeBlanc, S. E., Broccardo, S., Freitag, S., and
1242 Reid, J. S.: Above-aircraft cirrus cloud and aerosol optical depth from hyperspectral

1243 irradiances measured by a total-diffuse radiometer, *Atmos. Meas. Tech.*, 15, 1373–1394,
1244 <https://doi.org/10.5194/amt-15-1373-2022>, 2022.

1245 Payne, V. H., Drouin, B. J., Oyafuso, F., Kuai, L., Fisher, B. M., Sung, K., Nemchicka, D.,
1246 Crawford, T. J., Smyth, M., Crisp, D., Adkins, E., Hodges, J. T., Long, D. A., Mlawer, E. J.,
1247 Merrelli, A., Lunny, E., and O’Dell, C. W.: Absorption coefficient (ABSCO) tables for the
1248 Orbiting Carbon Observatories: version 5.1, *J. Quant. Spectrosc. Ra.*, 255, 1–16,
1249 <https://doi.org/10.1016/j.jqsrt.2020.107217>, 2020.

1250 Pilewskie, P., Pommier, J., Bergstrom, R., Gore, W., Howard, S., Rabbette, M., Schmid, B., Hobbs,
1251 P. V., and Tsay, S. C.: Solar spectral radiative forcing during the Southern African Regional
1252 Science Initiative, *J. Geophys. Res.*, 108, 8486, <https://doi.org/10.1029/2002JD002411>, 2003.

1253 Pincus, R. and Evans, K. F.: Computational cost and accuracy in calculating three-dimensional
1254 radiative transfer: Results for new implementations of Monte Carlo and SHDOM, *J. Atmos.*
1255 *Sci.*, 66, 3131–3146, 2009.

1256 Platnick, S., King, M. D., Ackerman, S. A., Menzel, W. P., Baum, B. A., Riédi, J. C., and Frey, R.
1257 A.: The MODIS cloud products: Algorithms and examples from Terra, *IEEE T. Geosci.*
1258 *Remote*, 41, 459–473, 2003.

1259 Reid, J. S., Maring, H. B., Narisma, G., van den Heever, S., DiGirolamo, L., Ferrare, R., Lawson,
1260 P., Mace, G. G., Simpas, J., Tanelli, S., Ziemba, L., van Diedenhoven, B., Brientjes, R.,
1261 Bucholtz, A., Cairns, B., Cambaliza, M. O., Chen, G., Diskin, G. S., Flynn, J. H., Hostetler,
1262 C. A., Holz, R. E., Lang, T. J., Schmidt, K. S., Smith, G., Sorooshian, A., Thompson, E. J.,
1263 Thornhill, K. L., Trepte, C., Wang, J., Woods, S., Yoon, S., Alexandrov, M., Alvarez, S.,
1264 Amiot, C., Bennett, J. R., Brooks, M., Burton, S. P., Cayan, E., Chen, H., Collow, A.,
1265 Crosbie, E., DaSilva, A., DiGangi, J. P., Flagg, D. D., Freeman, S. W., Fu, D., Fukada, E.,
1266 Hilario, M. R. A., Hong, Y., Hristova-Veleva, S. M., Kuehn, R., Kowch, R. S., Leung, G. R.,
1267 Loveridge, J., Meyer, K., Miller, R., Montes, M. J., Moum, J. N., Nenes, T., Nesbit, S. W.,
1268 Norgen, M., Novak, E., Rauber, R. M., Reid, E. A., Rutledge, S., Schlosser, J. S., Sekiyama,
1269 T. T., Shook, M. A., Sokolowsky, G. A., Stamnes, S. A., Sy, O. O., Tanaka, T. Y., Wasilewski,
1270 A., Xian, P., Xiao, Q., and Zavaleta, J.: The coupling between tropical meteorology, aerosol
1271 lifecycle, convection, and radiation, during the Clouds, Aerosol and Monsoon Processes
1272 Philippines Experiment (CAMP²Ex), *B. Am. Meteorol. Soc.*, *in review*, 2022.

1273 Ronneberger, O., Fischer, P., and Brox, T.: U-net: Convolutional networks for biomedical image

1274 segmentation, in: International Conference on Medical image computing and computer-
1275 assisted intervention, 234–241, Springer, https://doi.org/10.1007/978-3-319-24574-4_28,
1276 2015.

1277 Rothman, L., Jacquemart, D., Barbe, A., Chris Benner, D., Birk, M., Brown, L., Carleer, M.,
1278 Chackerian, C., Chance, K., Coudert, L., Dana, V., Devi, V., Flaud, J.-M., Gamache, R.,
1279 Gold- man, A., Hartmann, J.-M., Jucks, K., Maki, A., Mandin, J.- Y., Massie, S., Orphal, J.,
1280 Perrin, A., Rinsland, C., Smith, M., Tennyson, J., Tolchenov, R., Toth, R., Vander Auwera,
1281 J., Varanasi, P., and Wagner, G.: The HITRAN 2004 molecular spectroscopic database, *J.*
1282 *Quant. Spectrosc. Ra.*, 96, 139–204, <https://doi.org/10.1016/j.jqsrt.2004.10.008>, 2005.

1283 Schmidt, K. S., Pilewskie, P., Platnick, S., Wind, G., Yang, P., and Wendisch, M.: Comparing
1284 irradiance fields derived from Moderate Resolution Imaging Spectroradiometer airborne
1285 simulator cirrus cloud retrievals with solar spectral flux radiometer measurements, *J. Geophys.*
1286 *Res.*, 112, D24206, doi:10.1029/2007JD008711, 2007.

1287 Schmidt, S., Pilewskie, P., Mayer, B., Wendisch, M., Kindel, B., Platnick, S., King, M. D., Wind,
1288 G., Arnold, G. T., Tian, L., Heymsfield, G., and Kalesse, H.: Apparent absorption of solar
1289 spectral irradiance in heterogeneous ice clouds, *J. Geophys. Res.*, 115, D00J22,
1290 <https://doi.org/10.1029/2009JD013124>, 2010.

1291 Schmidt, S., Massie, S., Chen, H., Crisp, D., Kulawik, S., Chen, Y.-W., Merrelli, A., McDuffie, J.,
1292 Iwabuchi, H.: Uncovering the Mechanism for Trace Gas Spectroscopy Biases in the Vicinity
1293 of Clouds With the OCO-2 3D Radiative Transfer Satellite Radiance Simulator, *Atmos. Meas.*
1294 *Tech.*, *in prep.*, 2022.

1295 Song, S., Schmidt, K. S., Pilewskie, P., King, M. D., Heidinger, A. K., Walther, A., Iwabuchi, H.,
1296 Wind, G., and Coddington, O. M.: The Spectral Signature of Cloud Spatial Structure in
1297 Shortwave Irradiance, *Atmos. Chem. Phys.*, 16, 13791–13806, [https://doi.org/10.5194/acp-](https://doi.org/10.5194/acp-16-13791-2016)
1298 [16-13791-2016](https://doi.org/10.5194/acp-16-13791-2016), 2016.

1299 Spada, F., Krol, M. C., and Stammes, P.: McSCIA: application of the Equivalence Theorem in a
1300 Monte Carlo radiative transfer model for spherical shell atmospheres, *Atmos. Chem. Phys.*,
1301 6, 4823–4842, <https://doi.org/10.5194/acp-6-4823-2006>, 2006.

1302 Vermote, E. F., Roger, J. C., and Ray J. P.: MODIS Surface Reflectance User’s Guide, MODIS
1303 Land Surface Reflectance Science Computing Facility, Version 1.4, 1-35, 2015.

1304 Wood, J., Smyth, T. J., and Estellés, V.: Autonomous marine hyperspectral radiometers for

1305 determining solar irradiances and aerosol optical properties, *Atmos. Meas. Tech.*, 10, 1723–
1306 1737, <https://doi.org/10.5194/amt-10-1723-2017>, 2017.